CFD STUDY OF THE DEVELOPMENT OF INTER-SUBCHANNEL ISOTHERMAL LAMINAR FLOWS

CFD STUDY OF THE DEVELOPMENT OF INTER-SUBCHANNEL ISOTHERMAL LAMINAR FLOWS

By

Gujin Wang, B. Eng.

A Thesis

Submitted to the School of Graduate Studies

In partial Fulfillment of the Requirements

For the Degree

Master of Applied Science

McMaster University

MASTER OF APPLIED SCIENCE McMaster University
(Mechanical Engineering) Hamilton, Ontario

TITLE: CFD Study of the Development of Inter-Subchannel Isothermal Laminar Flows

AUTHOR: Gujin Wang, Bachelor of Engineering (McMaster University)

SUPERVISOR: Dr. Marilyn Lightstone
Dr. Stephen Tullis

NUMBER OF PAGES: Xiii, 86

Lay Abstract

Flow pulsation is important in nuclear reactor design and optimization because it enhances mixing in subchannel flows. This study is a computational fluid dynamics simulation of pulsating flows in nuclear subchannels on geometries with existing experiment data. It focuses on the evolution of flow pulsations. Separate origins of flow pulsations were observed in the simulations and their growth and interactions were discussed in detail.

Abstract

The design and optimization of nuclear reactors, specifically in the case of CANDU, involves the study of subchannel flows. The mixing inside the subchannels is crucial to the efficiency of heat transfer between the fuel rods and the coolant. Numerous studies have been done throughout the past few decades regarding the physics of subchannel flows, most of which being inside the turbulent regime.

Despite the fact that subchannel flows in nuclear reactors are turbulent in nature, studies have shown that flow pulsations inside subchannels can occur under laminar conditions. It is thus beneficial to study pulsations in laminar flows, as it avoids the complications of turbulent modeling, for a clear understanding of the cause and growth of the pulsations.

Laminar simulations of various experiments in subchannel flows were conducted in this study, with a focus on exploring the evolution of the pulsations. Initial developments of flow in different regions of the subchannels were observed along with their evolutions and interactions with each other. Qualitative and quantitative results were analyzed to give a better understanding of the flow pulsations in laminar condition.

Acknowledgement

This work would not be possible without the guidance and supervision of my supervisors Dr. Lightstone and Dr. Tullis. Their help to me was beyond academic but also personal when I lost my focus. I am deeply grateful for what they have done for me. I would also like to thank my parents for their continued trust and encouragement. University Network of Excellence in Nuclear Engineering (UNENE) provided financial support and is greatly appreciated.

Table of Contents

List of Figures

List of Tables

List of Abbreviations and Symbols

Letters:

x: spanwise direction

y: cross gap direction

z: streamwise direction

D: rod Diameter

δ: gap spacing

A: flow area

D_H: hydraulic diameter

L: domain length

T: temperature

V: volume

μ: dynamic viscosity

ρ: density

Re: Reynolds Number

St: Strouhal Number

β: blending factor

f: frequency

N: number of crossings

P: number of periods

λ: wavelength

τ: travel time of the centerline crossing particle

r: sample correlation coefficient

Superscripts:

$n+\frac{1}{2}$: start of timestep n

$n-\frac{1}{2}$: end of timestep n

Subscripts:

top: top gap

bot: bottom gap

ip: integration point

up: upwind

bulk: value based on bulk velocity

local: value based on local velocity

rms: root mean square

Y: mixing coefficient

Chapter 1 Introduction

1.1 Background

The Canadian developed CANDU (Canada Deuterium Uranium) power plants supply approximately 50 percent of Ontario's electricity [1]. The electricity generated is safe and clean compared to that from traditional power plants [1]. Figure 1.1 shows the overall flow of electricity generation and delivery with the CANDU reactor. Cylindrical uranium rods are used as fuel for the reactor. They are tightly packed into fuel rod bundles which then form fuel channels. The coolant heavy water flows inside the rod bundles and absorbs the heat generated by nuclear fission. The heated heavy water then goes through a heat exchanger and gives off heat to light water which powers the steam turbines to generate electricity. A diagram of the rod bundles can be seen in Figure 1.2. The fuel rods form subchannels where the coolant flows through. The thin black line in Figure 1.2 represents gaps between rods where mixing occur.

The correct prediction of the mixing rates between the subchannels is important in analyzing the temperature distribution inside the reactor and is crucial in safety analysis. Numerous studies, including the present study, are focused on the understanding of the fluid physics inside rod bundles for better assessment of the mixing rates between subchannels. In particular, oscillating flow between adjacent subchannels has been seen [2]. Although there have been considerable amount of experimental and numerical studies of the flow pulsations, the origin of them is still not clearly understood. These flow pulsations have been seen in laminar flows [3] as well as the high Reynolds number turbulent flows typical of reactors. Notably, the pulsations do occur in simplified geometries of even just two subchannels separated by a single gap [4], or geometries made of a rectangular duct containing a single rod [5].

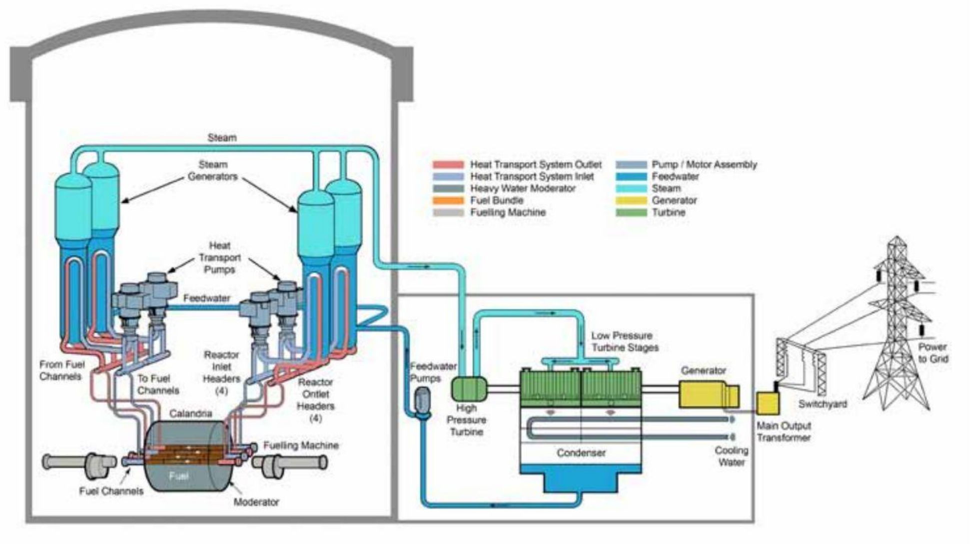

Figure 1.1 Overall plant flow diagram for a CANDU power plant from Enhanced CANDU 6 Technical Summary [6].

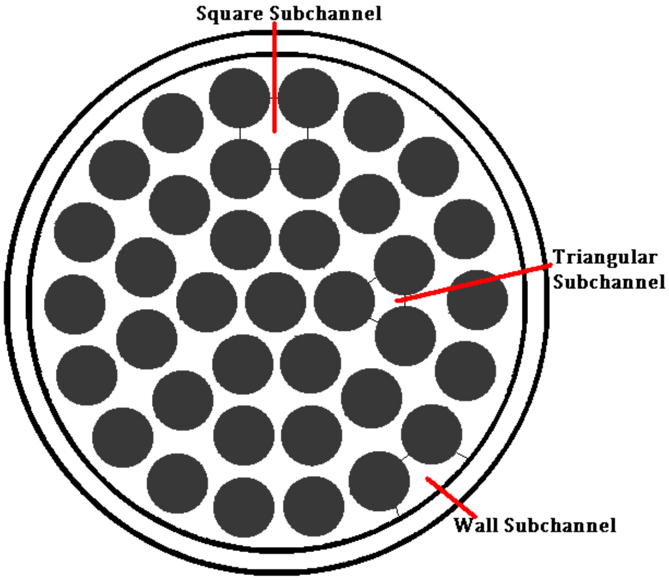

Figure 1.2 Cross section view of a 37-rod bundle from Eiff and Lightstone [7]. Coolant flows through the subchannels into the page.

1.2 Objectives of Research

The objective of this research is to simulate flows inside rod bundles on simplified geometries using CFD (computational fluid dynamics) in laminar conditions and gain knowledge of the growth and evolution of the pulsating flows inside rod bundles.

Specific goals of the research are:

1. Simulate the flow on the selected geometry using CFD.
2. Validate the simulation against experimental results using a Lagrangian method.

3. Study the growth and evolution of the quasi-periodic structures in laminar subchannel flows.
4. Study the interactions of the pulsations between two opposing gaps.
5. Analyze the flow features in different stages of the growth.

1.3 Structure of Thesis

This thesis is divided into five chapters.

Chapter 1 gives some background information on the purpose of the research and the objectives set to be completed.

Chapter 2 is a literature review of previous work on this topic including experimental and numerical investigations. The experimental works are categorized by the different physical phenomena, and the numerical works are categorized by different methodologies. It is worth noting that some works may belong to multiple categories, the dominant features of those works are considered when they were put in a certain section.

Chapter 3 is a detailed review of the methodologies employed in the present research, essentially a detailed flow chart to reproduce this work.

Chapter 4 gives results from the numerical simulations and discussion. It is logically organized by first looking at the development and growth of the flow, and then the features of the flow when in a statistically stationary state.

Chapter 5 concludes this research and gives recommendations for future works.

Chapter 2 Literature Review

2.1 Overview

This chapter presents a literature review on intersubchannel mixing including both experimental and numerical studies. The information presented here is arranged by the physical phenomena. Early research in this area mainly attributed the enhanced mixing to turbulent transport and secondary flows. However, later experiments suggested that those mechanisms were not sufficient to account for the enhanced momentum and heat exchange between subchannels. Research shifted towards quasi-periodic structures.

2.2 Experimental Investigations

2.2.1 Mean Flow

The behavior of the mean flow were one of the first primary focuses in investigating the enhanced mixing in intersubchannel flows. Geometrical characteristics were found to be the determining factors influencing the mean flow characteristics in an intersubchannel flow. The gap size in terms of pitch to diameter ratio is a notable parameter.

Eifler and Nijsing [8] investigated intersubchannel flow as early as 1966. They performed experiments on infinite triangular array of parallel rods in order to obtain information concerning the fluid flow and heat transfer in intersubchannel flows, and to establish a law to describe the velocity distribution normal to the rod surface. They found that the velocity vary with different wall distance and peripheral angle. Local friction factor also changes with different pitch to diameter ratio.

Ouma and Tavoularis [9] looked at turbulent air flow through a five-rod sector of a 37-rod bundle. Because of the geometrical complexity of the rod subchannel, they adapted a length scale more relevant than the hydraulic radius, the length scale being the distance between the channel's wall and the line of maximum velocity. As concluded in their research, the use of subchannel averages, like the case in many subchannel codes, in predicting the variation of local properties could lead to errors because of the non-uniformity of the aforementioned length scale.

Guellouz and Tavoularis [10] continued the research of Ouma and Tavoularis [9]. Using the same geometry, they measured the heat transfer coefficient and found that the local heat transfer coefficient was highly sensitive to pitch to diameter ratios at very narrow gaps.

Hosokawa, Yamamoto, Okajima and Tomiyama [11] used a particle image velocimetry (PIV) system to measure water flows in a two by two rod bundle and used the results as validation for their numerical simulations presented in the same paper. The measured results led the researchers to believe that the axial mean velocity along the line normal to the rod in the inner subchannel agreed well with the one-seventh power low. It was also noted that the velocity fluctuations in spanwise direction decreased in the rod gap.

2.2.2 Turbulent Transport

Turbulent diffusion was considered to be the cause of the intersubchannel mixing due to the fact that they are often positively correlated.

In 1967, Nijsing, Eifler, Delfau and Camposilvan [12] performed experiments on a 7-rod cluster with finned cladding. They used tracer injection to measure intersubchannel mixing. Single direction and two direction intersubchannel flows were both observed based on the boundary condition of the subchannels with helical fins. For smooth rods, the authors claimed that “turbulent diffusion is the sole mechanism responsible for intersubchannel mixing” due to the fact that mixing rate was relatively small.

Rehme [13] in 1977 performed experiments on a rectangular duct with four parallel rods. Eddy viscosity measurements in circumferential and radial directions were obtained, and were used to adjust the VELASCO code developed by Eifler and Nijsing [14]. There were significant discrepancies between the measurements and the predictions from VELASCO code. It was proposed that the assumption made in the code that eddy viscosity was constant across the radius was affecting the calculations. The measurements showed that eddy viscosity was position dependent. Renksizbulut and Hadaller [15] also tried to modify VELASCO based on their experimental result. Increased anisotropy in the gap regions produced results with close agreement. Wu and Rehme's experiment in 1990 [16] compared results with VELASCO code and found that it incorrectly predicted wall shear stress, the reason being its lack of modeling of cyclic momentum transport between neighboring subchannels.

Hooper's experiments [17] on a square duct containing six rods showed a departure of the turbulent structure from that in a pipe flow. The magnitude of departure was found to be strongly correlated with the pitch to diameter ratio. The magnitude of turbulent kinetic energy in the gap region increased as the pitch to diameter ratio decreased.

2.2.3 Secondary Flow

Although turbulent diffusion was seen as the sole underlying mechanism of the intersubchannel mixing by many researchers, numerous studies have also explored the possibility of turbulent secondary flow contributing to enhanced mixing rate.

Skinner, Freeman and Lyall [18] studied heat transfer between subchannels using a mass-transfer analogy on a seven-rod cluster. They used nitrous oxide as tracer for determining the mixing rate. Both smooth and roughened rods were used in the experiments. It was found that the diffusivity for momentum from different models were lower than the effective diffusivity in the gap region which suggested that the mechanism cannot be accounted for by turbulent diffusion alone. From their measurement and calculation, for one to draw a reasonable conclusion that intersubchannel mixing is caused by secondary flow it would need a secondary flow of the order of two percent for the smooth cluster and six percent for the roughened cluster. Although the results agreed well with smooth clusters as mixing increases with higher Reynolds number, the results for roughened clusters did not agree well in this perspective. Assumptions about roughened clusters not behaving as a fully roughened surface within the tested range of Reynolds number need to be made in order to justify the results.

Tachibana et al. [19] did experiments on a non-concentric annuli seven-rod cluster in 1969. Naphthalene sublimation was used in determining transport coefficient. The local heat transfer characteristics were found to be more complex than what would have been predicted by conventional correlations. A clear, almost sinusoidal periodicity was observed in the circumferential variation. It was concluded that the effect of secondary flow was important in obtaining more accurate prediction of the heat transfer coefficient.

Rowe et al. [20] studied the effect of flow channel geometry in rod bundle flows. Experiments were carried out on a square duct with various pitch to diameter ratios. Consistent with other researches, they concluded that pitch to diameter ratio is the most important geometric parameter in determining flow structure. Reduced gap spacing resulted in increased scale and frequency of flow pulsations. Secondary flows and other macroscopic flow processes were believed to be present in rod bundle flows but with small magnitudes.

Trupp and Azad [21] found a secondary flow with less than 0.5% magnitude of the bulk average axial flow in their experiments, which were performed on triangular array rod bundles in a wind tunnel. Magnitudes of secondary flows also varied with different pitch to diameter ratio and different Reynolds number. The researchers also believed that secondary flow played a large part in high mixing rates.

Seale [22] in the experiment conducted in 1982 measured a secondary flow with the magnitude of 1.5% of the bulk axial velocity. The experimental domain was a rectangular duct with two rods. The friction factor was found to be lower than that in a smooth circular pipe. An important conclusion from this experiment was that k-ε turbulence model for isotropic eddy viscosity combined with algebraic source for generating secondary flow was sufficient in calculation axial velocities and mean turbulence kinetic energies.

Renksizbulut and Hadaller [15] reported presence of secondary flows in their experiments on a six-rod duct. Distortion in the velocity profile suggested secondary flow in the corner subchannels but not in the wall and central subchannels. The magnitude of the secondary flow was not measured successfully and was deemed to be very small. It was also found that bulk flow in the central subchannel is similar to pipe flow with higher turbulence intensities. Contrary to flow structures being dependent on the pitch to diameter ratio suggested by hooper [17], the turbulent mixing between adjacent subchannels in this case was found to be insensitive to gap size.

Vonka [23] [24] also measured small secondary velocities in his experiments on four rods arranged in a triangular array. Secondary velocities were found to be independent of Reynolds number when non-dimensionalized with friction velocity. The magnitudes of the secondary velocities were less than 0.1% of the bulk velocity. Despite the fact that the secondary velocities were very small in magnitudes, Vonka concluded from experimental data that they contributed to about half of the total peripheral momentum transport and the remaining half caused by other turbulent transport mechanisms.

In summary, researchers considered the enhanced mixing rate in subchannel flows as a result of secondary flows. However, the typical magnitudes of secondary flows were very small in various experiments. The presence of secondary flows was little to non-existent in some experiments within the turbulent regime in non-circular duct. For example, Seale [25] conducted a series of experiments in 1978 in a wind tunnel with three configurations representing three pitch to diameter ratios. The results confirmed that the mixing rate in intersubchannel flows was considerably higher than predicted by simple diffusion theory. The higher mixing rate was attributed to the anisotropy in the gap region. The lack of significant distortions in the velocity and temperature contours suggested a lack of significant secondary flows.

2.2.4 Large Scale Eddies

Hooper and Rehme [2] reported results from experiments on a rectangular duct with four rods as well as a test section containing six rods in a square-pitch array. The two geometries represented the wall subchannel and interior flow region of a large array respectively. They examined the possibility of multiple mechanisms that could have been the cause of the large-scale structures with the conclusion that intersubchannel instability was the generating mechanism.

Rehme [26] concluded from his experimental results on four rod packed rectangular duct that the structure of turbulence in closely packed subchannels differed widely from flow through circular pipes. This effect was seen to be more prominent in and near the gap regions. There was cyclic momentum exchange by “a pulsating flow” between neighboring subchannels. Wu and Rehme [16] later performed similar experiments. The slight difference was that the four rods were arranged asymmetrically in the channels. The results once again confirmed the deviation of the turbulence structures from those in circular pipes.

Möller [27] performed experiments to determine the origin of the quasi-periodic fluctuating velocities on four parallel rods in a rectangular duct. It was found that the frequency of the quasi-periodic pulsations did not vary with Reynolds number, but rather was dependent on the pitch to diameter ratio. Based on the observations an empirical equation was proposed to calculate the frequency of the quasi-period pulsations in terms of Strouhal number (a dimensionless number describing the oscillating flow mechanics, St = fD/u) (equation 2.1). Möller also proposed a phenomenological model to explain the quasi-periodic pulsations. The model mainly attributed the cross gap flow to large scale eddies. He stated that under ideal conditions the vorticity fields on two sides of the gap would be identical and the eddies generated on both sides would be obstructions to one another. However, because the ideal conditions could not exist, the motions of the eddies were not obstructed and hence the quasi-periodic cross gap flow.

$$St^{-1} = 0.0808\left(\frac{P}{D} - 1\right) + 0.056 \qquad \text{(Eq. 2.1)}$$

Adapted from Möller [27]**.**

Möller [28] continued his research by measuring the mixing coefficient on the same geometry. In his calculations for mixing velocities it was assumed that only the eddies that caused the peak frequency were responsible for the mass flow across the gap and small eddies were neglected, and he obtained an empirical equation for the mixing coefficient based on pitch to diameter ratio of the gap. This empirical equation, along with other equations for mixing coefficient was later reviewed by Rehme [29]. Rehme criticized the assumptions Möller and stated that the flow pulsations were not caused by large scale eddies of one size but rather a spectrum of eddies. Rehme then re-fitted Möller's data and obtained a more accurate empirical relationship. Rehme also concluded that the periodic flow pulsations were the main reason for the natural mixing between subchannels of rod bundles and secondary flow did not contribute significantly.

Wu and Trupp [30] [31] in their experiments on a trapezoid bounded subchannel with a single rod found a region with high axial turbulence intensity remarkably different from normal boundary layers near the rod-to-wall gap, and it increased with decreasing pitch to diameter ratio. The increase however did not obstruct the motion of eddies in small gaps. Secondary flow was found to be an important transport process within the subchannel itself but not the cross gap flow. Large scale eddies were believed to be the mechanisms behind the cross gap mixing. And the frequency of the eddy motion was dependent on the geometry similar to Möller's findings [27]. Wu later conducted experiments [32] specifically designed to compare cross gap transport with respect to symmetric versus asymmetric subchannels by placing the rod asymmetrically. Similar to symmetric subchannels there were strong periodic eddy motion in the bottom gap. However, in the asymmetric case the lack of clear peak in side gaps indicated the magnitude of intersubchannel transport was strongly geometry dependent.

Meyer and Rehme [4] performed experiments on two rectangular ducts connected by a rectangular gap (Figure 2.1). They observed a “strong large-scale quasi-periodic flow oscillation” of which the Strouhal number was dependent on the pitch to diameter ratio of the geometry and independent of the Reynolds number.

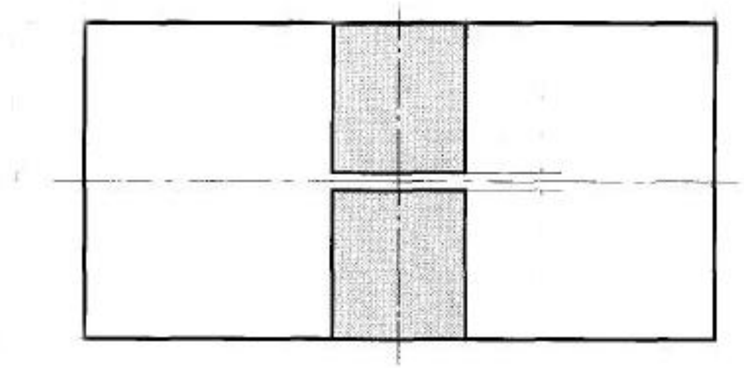

Figure 2.1 Two rectangular ducts connected by a rectangular gap. Adapted from Meyer and Rehme [4].

Krauss and Meyer [33] [34] performed experiments on a heated 37-rod bundle. Results indicated the existence of large-scale temperature pulsations with quasi-periodic velocity fluctuations of identical frequency. It was found that the distribution of wall shear stress and the dimensionless wall temperature varied over a wider range in a channel with smaller pitch to diameter ratio.

Guellouz and Tavoularis [35] [36] studied turbulent flow in a rectangular duct containing a single rod (similar to the geometry of present study). The rod was placed such that the subchannels were symmetric whereas the gaps were not. Coherent structures were observed with symmetric subchannels, leading to the conclusion that the structures were not the result of subchannel asymmetry, but rather due to instability caused by the narrow gap. It was proposed that the quasi-periodic structures were similar to von Karman vortex shedding. The coherent structures were found to be “highly correlated” by Baratto et al. [37] in their experiments on a 5-rod bundle. The change of frequency in one gap could lead to same change to frequency in the other gap.

Silin and Juanicó [38] measured the turbulent mixing on a circular pipe containing three rods. The obtained mixing rate had the same Reynolds number index as derived supposing an effective eddy diffusivity through the gap, leading to the implication that viscosity “affects large scale flow pulsations in a manner similar to circular duct turbulence”.

Gosset and Tavoularis [3] conducted experiments on a rectangular duct containing a single rod under laminar flow conditions. Flow visualization was achieved by dye injection. Different Reynolds numbers as well as different pitch to diameter ratios were tested. For each geometric setup a critical Reynolds number was determined below which no pulsation would occur due to the dominant presence of shear. Measurements on frequencies of the pulsations were made by observing the number of changes of dye streaks within the observation time. Wavelengths were determined by combining the velocity and the frequency of the wave. The experiment was strong evidence that quasi-periodic structures in subchannel flows can occur under laminar conditions. Piot and Tavoularis [39] later performed experiments on eccentric annular channels under laminar flow conditions. The study had an emphasis on linear stability analysis. The existence of two inflection points indicated instability of two shear layers forming on either side of the gap. Choueiri and Tavoularis [40] [41] later performed experiments on the same geometry using LDV and PIV. The researchers separated the domain into three regions based on the state of development of the quasi-periodic structures: the entrance region, the fluctuation growth region and the rapid-mixing region. Vortex streets were observed and were attributed to the instability caused by two mixing layers at the gap edges. The effects of different aspects of the flows on the generations of the quasi-periodic structures were also examined. Stronger management of inlet conditions led to delayed onset of periodic motions. Combinations of eccentricity and Reynolds number yielded different outcome of the flow. For small Reynolds number small eccentricity the flow remained stable and no periodic motions were detected. Larger eccentricity was required for cases with larger Reynolds number to form a quasi-periodic motion.

Mahmood, Rohde, van der Hagen and Mudde [42] experimented on two rectangular ducts connected by a curved wall gap. Their experiments included both turbulent and laminar results. Coherent structures were observed under both conditions and increased the mixing rates substantially.

2.3 Numerical Investigations

2.3.1 Reynolds Averaged Navier Stokes (RANS)

Early numerical research into intersubchannel mixing considered steady Reynolds averaged Navier Stokes to account for the effects of turbulence.

Seale [43] did numerical simulations with k-ε turbulence model, and used his own experiments [25] as validations. There were significant discrepancies between the computed results and the experimental results due to the use of isotropic effective diffusivity. However, difference in computed temperature distribution with or without the secondary flows was insignificant. It was concluded that secondary flow, although distorting the velocity and temperature profiles, had no major role in the momentum and energy transfer through the gaps. Rock and Lightstone [44] used the same experiment by Seale as validation for their simulation. An isotropic k-ε turbulence model was applied. The simulation predicted wall shear stress and friction factor adequately. However the isotropic nature of the turbulence model led to a discrepancy in the prediction of turbulent mixing. The researchers suggested that a turbulence model able to capture anisotropic nature of the flow was needed to improve the prediction of mixing. Suh and Lightstone [45] continued the research using both *k*-*ε* turbulence model and Reynolds stress model. Results were compared against experimental results by [29]. Reynolds stress model better predicted the velocity profile. Both turbulence models were not able to adequately capture the quasi-periodic structures.

Wu [46] simulated flow in a trapezoidal channel containing a rod using an algebraic stress model with *k*-*ε* turbulence model. Good agreement between the simulation and the experiments [30] was achieved after an anisotropy factor was introduced.

Lee and Jang [47] simulated a smallest symmetry segment of a subchannel which is 1/6 of a triangular array subchannel using a nonlinear *k*-*ε* turbulence model. The results were then compared to Carajilescov and Todreas [48]. The predictions agreed reasonably well with the exception of turbulent stress in the gap region. This study did not predict the large scale cross gap flow very well. The researcher concluded that special modeling of the large scale cross gap eddies were required in order to accurately predict the turbulent stress.

Horváth and Dressel [49] performed simulations on square arrayed rod bundles and used data from Hooper [17] as validation. They compared the effects of different meshes and turbulence models. Amongst the turbulence models examined, Reynolds stress models were proved to have captured the flow with greatest accuracy.

Hosokawa et al. [11] performed simulation on a 2 by 2 rod bundle and used their own experiments published in the same paper as validation. Standard k-ε turbulence model and Launder-Sharma k-ε turbulence model were used in the simulation. The predictions were somewhat in agreement with the experiments with standard k-ε model closer to the measurements. The lack of anisotropy in both turbulence models were the causes for the errors in prediction.

2.3.2 Unsteady Reynolds Averaged Navier Stokes (URANS)

Many researchers have suggested that Reynolds Averaged Navier Stokes are not sufficient in simulating pulsating flows, as RANS lacks the accuracy in predicting time dependent nature of the flow [50], and would sometimes require added empirical modeling for better agreement [51]. Unsteady Reynolds Averaged Navier Stokes in this case has advantages over RANS and has gained popularity in numerical investigation of subchannel pulsating flows.

Chang and Tavoularis did URANS numerical simulations on two different types of geometries. Their first set of simulations [51] [52] [53] was on the geometry of

Guellouz and Tavoularis [35] [36] (rectangular duct containing a single rod). The simulations were initiated using RNG *k*-*ε* turbulence model to avoid divergence. The results were then used as initial input in the actual simulation with Reynolds stress model. They observed the existence of coherent structures, most importantly in the gap regions where they "accounted for 60% of the total kinetic energy". By introducing a heat flux from the rod it was found that the coherent structures were significant in heat transfer in a rod-wall gap region, they increased the transport across the gap but also resulted in temperature and heat transfer coefficient fluctuations. The simulations also included varying gap sizes. The temperature fluctuations and turbulent kinetic energy in the gap regions increased as the pitch to diameter ratio was decreased, until a minimum gap size was reached for each Reynolds number. The dominant viscous effects in critical gap sizes would damp out the cross gap flow. Another simulation [54] by Chang and Tavoularis on the first type of geometry employed different turbulence models and made comparisons between the models. It was concluded that large eddy simulation reproduced the most accurate results. URANS simulation with Reynolds stress model was also found to generate good agreements with the experimental data. Chang and Tavoularis' second set of simulations [55] simulated the experimental work of Ouman and Tavoularis [9] (5-rod section of a 37-rod bundle. Because of the limitations of experimental setups the simulations were chosen to represent the full 37-rod bundle rather than the 5-rod experiment setup. Reynolds Stress Model was used in their simulation. They found a consistent spacing between pairs of coherent structures by utilizing Q criterion, from which they concluded that the coherent structures were connected to each other and formed a network of vortices that surrounded all the rods. The simulated Strouhal number and the measured Strouhal number from the experiments did not agree well, granted that the experimental work was done on a partial geometry that was only a section of the entire domain and without the center rod. Nevertheless, the results that were in agreement showed that relatively inexpensive CFD methods can be used to study intersubchannel coherent structures on complex geometries with certain degree of accuracy.

Merzari et al. [50] ran simulations on two different geometries. Firstly, a large eddy simulation on two rectangular ducts connect by a narrow gap similar to the geometry of Lexmond et al. [56]. Secondly, URANS simulations on a tight-lattice bundle similar to the geometry of Krauss and Meyer [34] but with fewer rods. Coherent structures were identified in their simulations. By comparing results from RANS and URANS the researchers concluded that unsteady simulations were necessary in predicting pulsating flows. The results also suggested that anisotropic modeling yielded more accurate results than isotropic modeling.

Home et.al.[57] used the Spalart-Allmaras (SA) model to simulate flow pulsations in a twin subchannel geometry. The SA model is calibrated for prediction of unsteady aerodynamic flows where vortex formation is present. Meyer and Rehme's experiments [4] were used as validation for this numerical work. The comparison between SA model and k-ε was made and it was found that SA better captured the quasi-periodic structures in terms of frequency. SA model being anisotropic, could not predict secondary flows accurately in this case. However, typical magnitudes of secondary flow are extremely low in rod bundle geometries as discussed in 2.2.3. The researchers concluded that SA model could be suitable in simulating flows in rod bundle geometries. Home and Lightstone [58] continued their research by using a hybrid unsteady Reynolds-Averaged Navier-Stokes/Large eddy simulation method, more specifically a shear stress transport (SST) based detached eddy simulation (DES) described by Strelets [59]. The DES-SST model was first studied on a fully developed turbulent channel flow by Home et al. [60] to ensure its applicability. The model captured the nature of the flow with excellent agreement, with the predicted and measured peak frequency of the large scale structure being 68.4 Hz and 68 Hz respectively. Instability played a large role in the origin of the vortex streets. The location of instability was found to be near the gap edge region where the velocity of the flow was inflectional in nature.

Instability caused by different flow resistances was identified by many researchers to be the origin of the quasi-periodic structures. Yan et al. [61] took a new approach in simulating the large scale structures. They omitted the narrow gap that was present in almost all the research regarding subchannel pulsations. Instead, they added different surface roughness to different parts of a flat rectangular duct. The surface with higher roughness, as one might expect, would have the same effect as the narrow gap as they both offered higher flow resistances than the rest of the duct. URANS with Reynolds stress models were utilized in the simulations. Their results showed large scale quasi-periodic pulsations without the presence of the narrow gap which in turn added to the point that instability contributed to intersubchannel flow pulsations.

Chettle [5] numerically investigated Gosset and Tavoularis' experiments [3] in laminar flow conditions. The characteristics of the simulated top gap pulsations roughly matched those found in the experiments, although the methods of obtaining the frequencies of the pulsations differ with the ones used in the experiments. And it was found that the flow throughout the domain is more complex than just top gap pulsations.

2.4 Summary

Different aspects and hypothesis were studied in the field of intersubchannel thermal mixing. The influence of geometrical characteristics to the mean flow, turbulent diffusions, turbulent secondary flows and large scale eddies were all milestones along the history of intersubchannel thermal mixing research. None of these mechanism alone can describe the underlying mechanics of the intersubchannel thermal mixing fully without discrepancies. Majority of the previous research also had a focus on turbulent flows. But as it stands, the underlying mechanism for generating quasi-periodic structures is not limited to turbulent flows.

Research on development and interactions of the periodic structures are also limited due to the difficulties in studying these aspects in turbulent flows. Studies in laminar flows can prove to be useful in understanding the nature of the pulsations. As a continuation of the work of Chettle [5], this study is going to be a CFD study primarily focusing on the geometry of Gosset and Tavoularis [3] and in laminar flow conditions. The purpose of using the this geometry is to help understand and focus on the development of the pulsations and cross flow complexity seen by Chettle [5], and to better compare the measured flow characteristics.

Chapter 3 Methodology

3.1 Geometry

The geometry studied here is a rectangular duct with an off-centered cylindrical core, which simulates two subchannels and two gap regions. It is the same geometry studied by Gosset and Tavoularis experimentally [3] hence providing a good basis for validating the numerical work. A cross section view of the geometry is shown in Figure 3.1. The length of the domain is 1.168 m. A summary of key features of the geometry is presented in Table 3.1. The cylindrical core is placed asymmetrically to simulate two gaps with different pitch to diameter ratios.

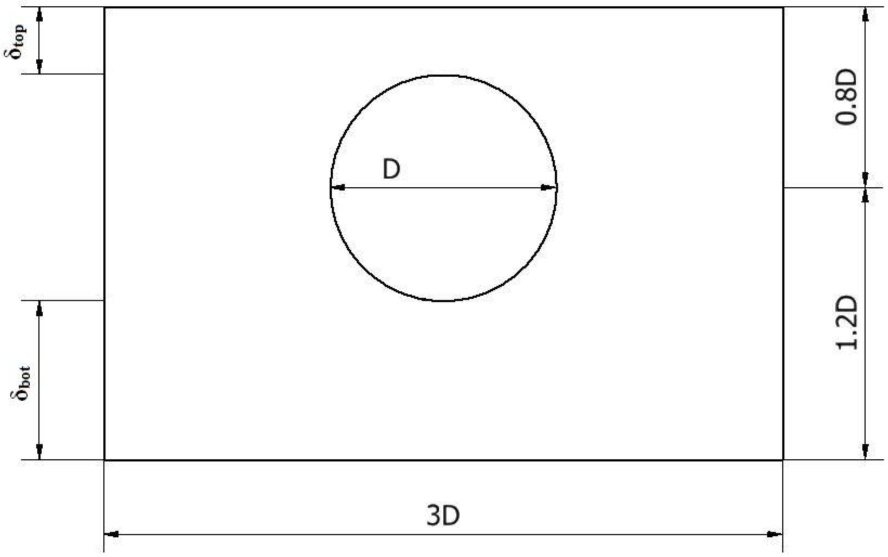

Figure 3.1 Cross section of the studied geometry by Gosset and Tavoularis [3]. Flow direction is into the page.

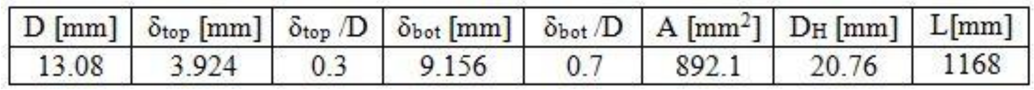

D [mm]	δ_{top} [mm]	δ_{top} /D	δ_{bot} [mm]	δ_{bot} /D	A [mm^2]	D_H [mm]	L[mm]
13.08	3.924	0.3	9.156	0.7	892.1	20.76	1168

Table 3.1 Summary of key features of the geometry. D is the diameter of the rod. δ is the distance from the rod edges to the wall of the duct. A is flow area. D_H is hydraulic diameter. L is the domain length.

3.2 Simulation Details

The simulations were performed using the commercial software ANSYS CFX v14.0 on a local workstation and on SHARCNET.

This section provides a detailed description of the numerical simulation and modeling of the geometry selected for this study, validations of the methodology are also presented.

3.2.1 Fluid Properties

The working fluid in all simulations is water with its properties listed in Table 3.2, and it is considered incompressible and isothermal for the scope of this research.

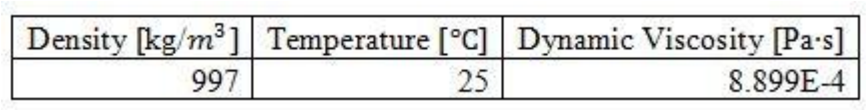

Density [kg/m^3]	Temperature [°C]	Dynamic Viscosity [Pa·s]
997	25	8.899E-4

Table 3.2 Fluid Properties.

One way coupled water particles with a diameter of 1e-6 m were injected at the center of the top gap 0.57L downstream of the inlet at the rate of one per timestep. The particles were set with a zero initial velocity. Combining the rate of the particle injection and the size of the particles the mass flow rate of the particles is

1.044e-14 kg/s which is insignificant compared to a mass flow rate of 2.75e-2 kg/s in the case of Re=718 for example. It is safe to assume the particle injection would not affect the flow itself.

3.2.2 Mesh and Independence

The mesh used in this study is a combination of structured rectangular mesh close to the duct wall and an o-grid mesh around the rod as shown in Figure 3.2. The perimeters of the rectangular duct and that of the rod are boundaries. The mesh is designed this way such that the resolution in the gap is fine enough to capture the flow details while the resolution in the subchannel is not too demanding for computing power. The domain length as discussed above is 1168 mm which is evenly divided into 0.75 mm-element. There are 2772 nodes on the cross section. The total number of nodes is 4316928. A sampling frequency was determined by multiplying the expected frequency from the experimental work [3] by 100. Timestep was set to be the inverse of the sampling frequency, which gives a timestep of 0.05, 0.04 and 0.03 seconds for Re=718, 900 and 955 respectively.

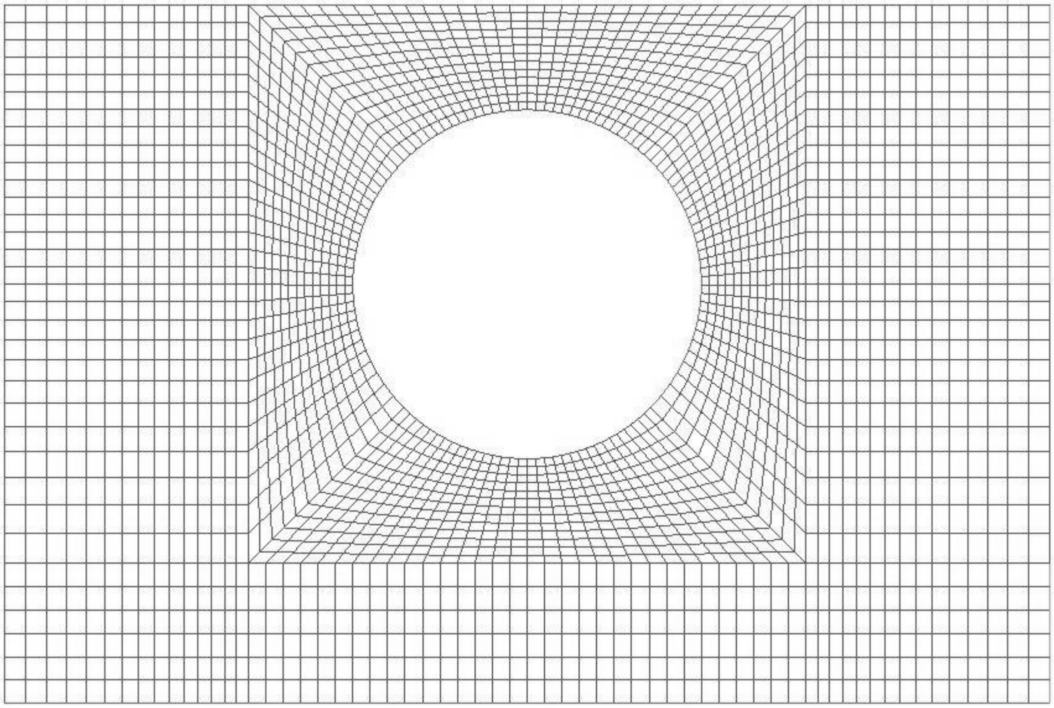

Figure 3.2 Cross section of the mesh used in the simulations.

Mesh independence tests were performed on a finer mesh which was obtained by doubling the number of nodes in every direction. Timestep independence test was also performed by doubling the sampling frequency.

Spanwise velocities of several monitor points were traced in order to compare the effect of the grid spacing and size of the timestep. The monitor points were taken to be the middle of the gap, edge of the rod and half way between the previous two points for both the top and bottom gaps. An illustration of locations of the monitor points is shown in Figure 3.3.

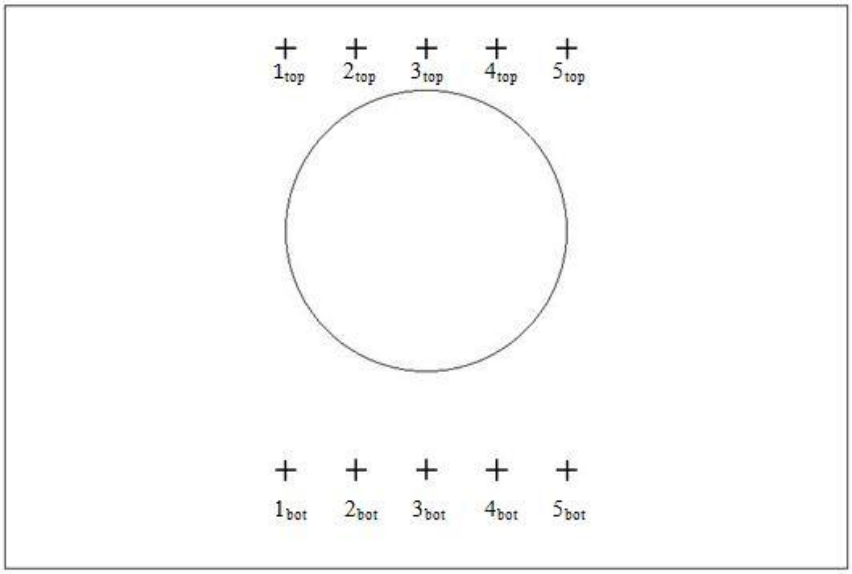

Figure 3.3 Locations of monitor points for independence tests.

Root mean square values of the spanwise velocities were used to evaluate the effect of size of the mesh and timestep. The results are tabulated in Table 3.1.

	1_{top}	2_{top}	3_{top}	4_{top}	5_{top}	1_{bot}	2_{bot}	3_{bot}	4_{bot}	5_{bot}
Base Grid u_{rms} [mm]	2.85	4.48	5.38	4.41	2.71	3.12	3.67	3.83	3.72	3.16
Spatial u_{rms} [mm]	2.80	4.60	5.31	4.50	2.70	3.11	3.54	3.78	3.88	3.04
Spatial Difference %	1.59	2.73	1.34	2.02	0.45	0.39	3.59	1.26	4.43	3.93
Temporal u_{rms} [mm]	2.75	4.33	5.40	4.37	2.71	3.21	3.54	3.92	3.83	3.27
Temporal Difference %	3.43	3.29	0.40	0.91	0.12	2.82	3.48	2.31	2.91	3.51

Table 3.3 Summary of spanwise velocity trace on monitor points for different mesh and timestep sizes

The percentage difference in root mean square of spanwise velocity resulting from halving the size of the meshes and timestep is 5.31% and 3.48% at maximum respectively. It is thus safe to conclude that the mesh and timestep used in the simulations are adequate to yield statistically similar signals. However, the quasi-periodic behavior of the pulsations needs to be looked at with different mesh sizes and timesteps. Figure 3.4 and Figure 3.5 are Fast Fourier Transforms of spanwise velocity from 3_{top} and 3_{bot} respectively. The different setups yield good agreement in frequency spectrum.

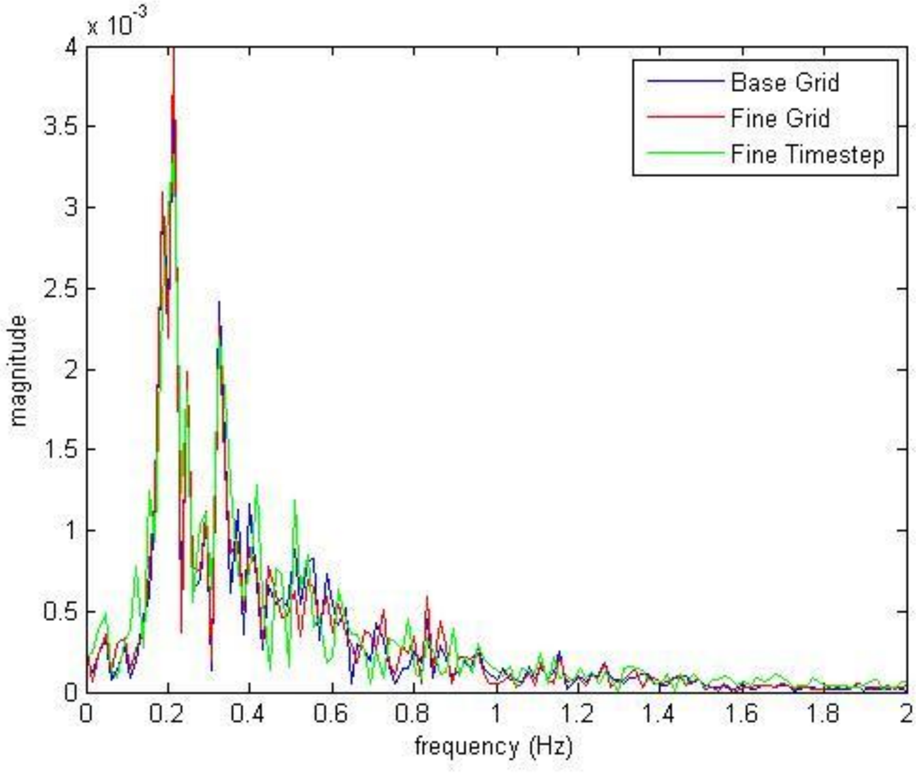

Figure 3.4 FFT of 3_{top} with different setups.

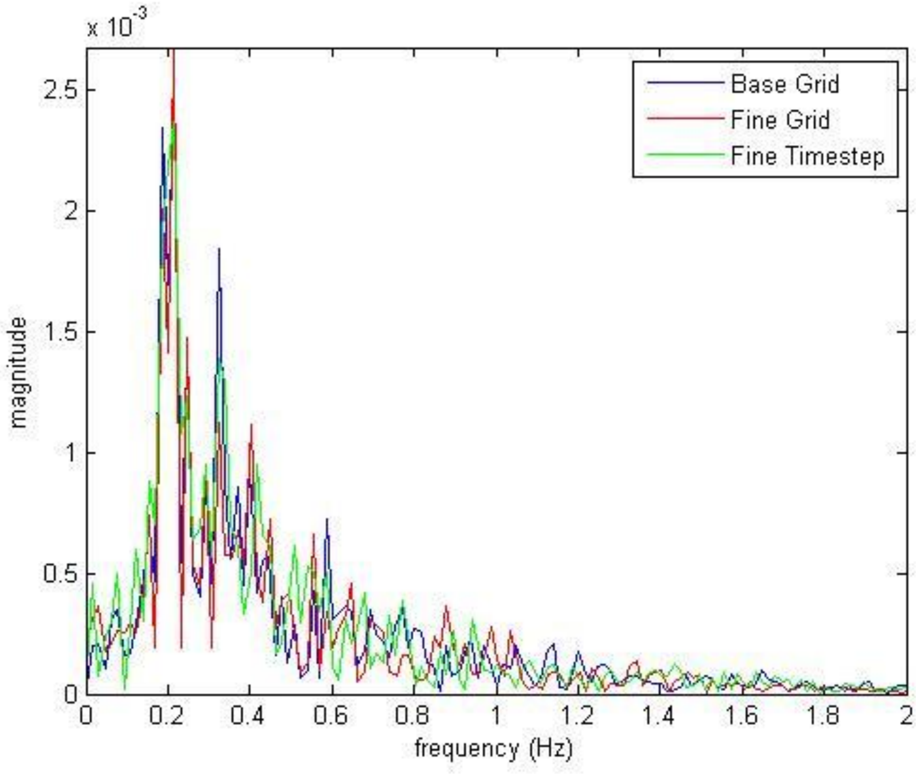

Figure 3.5 FFT of 3_{bot} with different setups.

As a result of above comparison, the mesh and timestep used in the simulations are adequate for the scope of this study.

3.2.3 Governing Equations

The governing equations solved are incompressible continuity equation and Navier-Stokes equation. As per discussed in Chapter 2 subchannel pulsations can occur in laminar flows . The simulations are based on the experiments with laminar flow conditions hence no turbulence model is considered. Thermal energy equations are not considered as the flow is isothermal. In equations 3.1 and 3.2, ***u*** is the velocity, p is pressure, ρ is the density of the fluid, $\mathbf{g}$ is the body acceleration per unit mass, and μ is the dynamic viscosity of the fluid.

The continuity equation

$$\nabla \cdot \mathbf{u} = 0 \qquad \text{(Eq. 3.1)}$$

The momentum equation

$$\rho \frac{D\mathbf{u}}{Dt} = -\nabla p + \rho \mathbf{g} + \mu \nabla^2 \mathbf{u} \qquad \text{(Eq. 3.2)}$$

3.2.4 Details of Numerical Setups

The simulations were performed using ANSYS CFX v14. It employs an element-based finite volume method. Fluid properties are stored at mesh nodes and a control volume is constructed around each node. The governing equations are integrated over each control volume. Volume integrals with divergence and gradient operators are transformed into surface integrals using Gauss' Divergence Theorem. Volume integrals are then discretized within each element sector belonging to the control volume. Surface integrals are discretized at integration points at the center of each surface segment. The resulting system of equations is then solved iteratively with a multigrid approach to enhance the convergence behavior of the solver [62].

Advection Scheme

High resolution advection scheme is used in the approximation of the integration point values based on the nodal values. Equation 3.3 is the equation ANSYS CFX uses in determining the integration point values [62], where $\emptyset_{ip}$ is the integration point value, $\emptyset_{up}$ is the upwind nodal value, and $\boldsymbol{r}$ is the vector from upwind node to the integration point. Different advection schemes are set apart by different values of blending factor β.

$$\emptyset_{ip} = \emptyset_{up} + \beta \, \nabla\emptyset \cdot \Delta\boldsymbol{r} \qquad \text{(Eq. 3.3)}$$

For each integration point around a node, a blending factor β is computed such that the $\emptyset$ value does not exceed the boundary of $\emptyset_{min}$ and $\emptyset_{max}$. Then the minimum β of all the surrounding integration points is taken to be the β value for the particular node. The blending factor β is designed to be as close to 1 as possible without introducing new extremes, and is not permitted to exceed 1 [62]. High resolution scheme was shown to perform well in computing subchannel flows by previous research [57].

Transient Scheme

For incompressible flow with non-deforming mesh, Equation 3.4 is used as the approximation of transient terms for the nth timestep.

$$\frac{\partial}{\partial t}\int_V \emptyset \, dV \approx V\,\frac{\emptyset^{n+\frac{1}{2}}-\emptyset^{n-\frac{1}{2}}}{\Delta t} \qquad \text{(Eq. 3.4)}$$

The transient scheme used in the simulations is second order backward Euler scheme where the start and end of timestep values are approximated by Equations 3.5 and 3.6 respectively. The transport value is estimated based on two previous values in time.

$$\emptyset^{n-\frac{1}{2}} = \emptyset^{0} + \frac{1}{2}\left(\emptyset^{0} - \emptyset^{00}\right) \qquad \text{(Eq. 3.5)}$$

$$\emptyset^{n+\frac{1}{2}} = \emptyset + \frac{1}{2}\left(\emptyset - \emptyset^{0}\right) \qquad \text{(Eq. 3.6)}$$

Second order backward Euler scheme provides a robust and conservative approximation of the transient terms and has no timestep size limitation [62].

Boundary and Initial Conditions

The boundary conditions at the wall of the duct and the rod are set to be non-slip wall with zero velocity. Periodic boundary conditions are set at the inlet and outlet of the duct with a specified mass flow rate for each of the Reynolds numbers. Initial guess of zero velocities throughout the entire domain was applied to a short domain with the same cross section and mesh density. After a steady non-pulsating velocity profile has been achieved, the velocity profile was then used as the initial condition for the actual simulation.

Chapter 4 Results and Discussions

This chapter is divided into two main sections. The first section examines the evolution of the quasi-periodic pulsations in the rectangular duct containing a single rod. The second part of this chapter is focused on the Lagrangian based method developed for the purpose of both validation and additional understanding of the characteristics of the flow pulsations.

4.1 Evolution of Pulse Trains

To better understand the generation of quasi-periodic structures in subchannel flows, the temporal progression of the flow from a purely axial flow to a statistically stationary state is examined. A single case with a Reynolds number of 718 and gap spacing of $\delta_{top}/D = 0.3$ and $\delta_{bot}/D = 0.7$ is investigated here.

The simulation was started from a fully developed axial velocity profile, which is the steady flow solution with the constraint of zero streamwise velocity gradients. The velocity profiles in the top and bottom gap can be seen in Figure 4.1. As expected, the solution shows a clear symmetry with high velocities in the subchannel and a significant reduction in the velocities in the gap regions. The inflection points on the velocity profiles are located at the edge of the rod in the spanwise direction, and can cause instability in the flow.

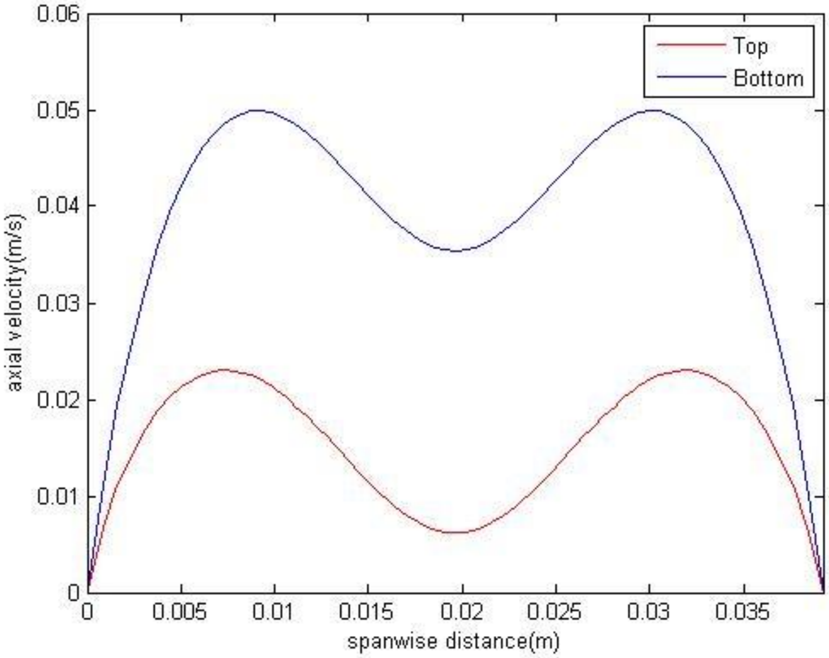

Figure 4.1 Fully developed steady axial velocity profile on lines in spanwise direction at center of the gaps Re=718.

Given this initial flow field, the transient solution rapidly develops very small disturbances to the flow in the form of spanwise flow through both the top and bottom gap. A rough measure of the growth of the spanwise flow is shown in Figure 4.2.

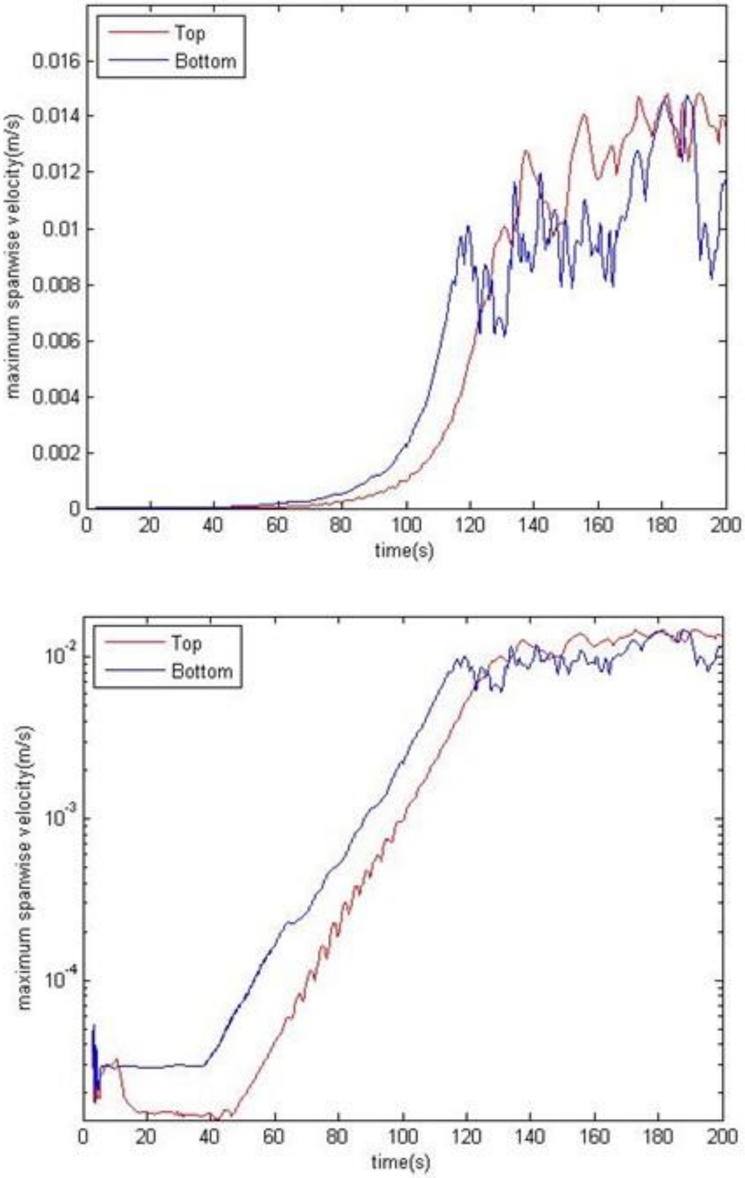

Figure 4.2 Maximum spanwise velocities on planes through the top and bottom gaps for Re=718 plotted on normal scale and semi log scale.

The magnitude of the spanwise velocities evolves at different rates through time. So it is reasonable to look at the evolutions of the pulsations based on different stages in time.

4.2 Early Stage Evolution

The early stage of the quasi-periodic structures evolution can be identified as time before roughly 120 seconds. This stage is characterized by the independent growth of the top and bottom gap flows with higher spanwise velocities in the bottom gap.

The onset of spanwise flow can be clearly seen as trains or wave packets of roughly 4-6 periodic fluctuations developing independently in the top and bottom gaps in Figure 4.3. A spanwise velocity plot of the instance can be seen in Figure 4.4. At this very early onset time (t=31.05s) the magnitude of the spanwise fluctuations is very small, with magnitudes of one thousandth of the streamwise velocity.

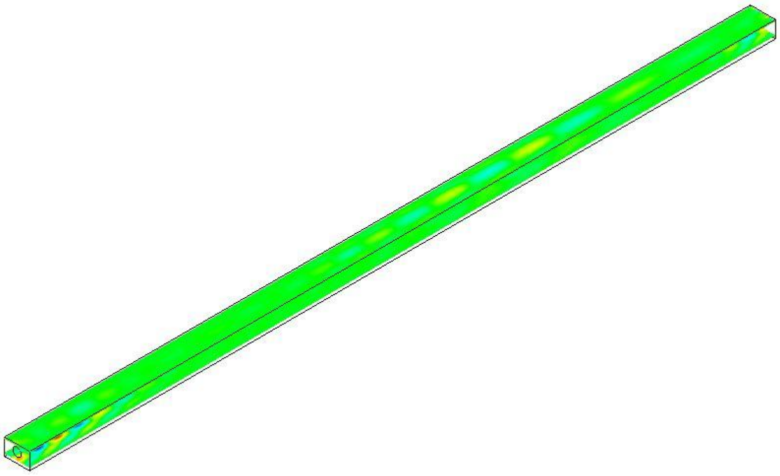

Figure 4.3 Contour plot of spanwise velocities in the top and bottom gap regions at 31.05 seconds.

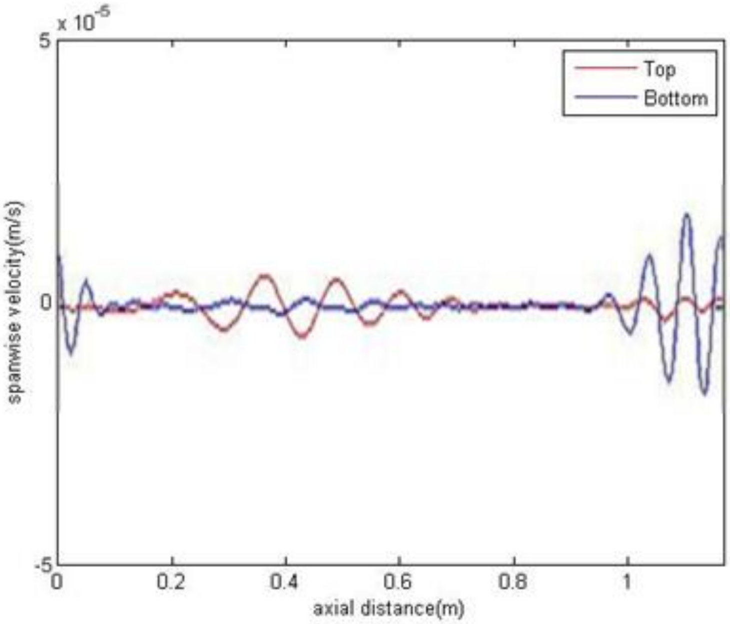

Figure 4.4 Spanwise velocities in the top and bottom gap regions at 31.05 seconds.

There are two trains present in each of the gaps, a larger or primary pulse train, and a weaker secondary pulse train that appears to be directly related to the primary pulse train from the other gap. The primary bottom gap fluctuations have larger magnitudes and shorter wavelengths than the primary top gap fluctuations as can be seen in Figure 4.4. The primary pulse trains maintain a constant group structure with their phase velocity approximately 1.5 times the group velocity, where the group velocity is defined by the velocity of the envelope of the pulse structure and the phase velocity is the velocity of the phase propagating through space. The bottom gap primary fluctuations have a higher group velocity than that of the top gap fluctuations. The group and phase velocities of both top and bottom pulse trains are significantly higher than the average fluid flow velocities in the gaps. At this time the streamwise extent of the primary pulse trains is approximately 0.6m and 0.4m for the top and bottom gaps respectively. These are isolated primary pulse trains and it is not clear whether multiple isolated pulse trains would occur in a longer simulated domain. The top and bottom pulse trains continue to grow in time. This growth is both in the magnitude of the pulse train cross flow velocities and in the axial extent of the pulse trains. The secondary pulse trains in the bottom gap have roughly the same wavelength, phase and group velocity of the top original pulse train and vice versa. The secondary pulse trains being directly related to the original pulse trains in the other gap, behaves like an “echo” of the original pulse trains. The characteristics of the gap pulse trains in early stage are summarized in Table 4.1. The top gap primary frequency is similar to that found in Chettle [5] which was also 0.21Hz.

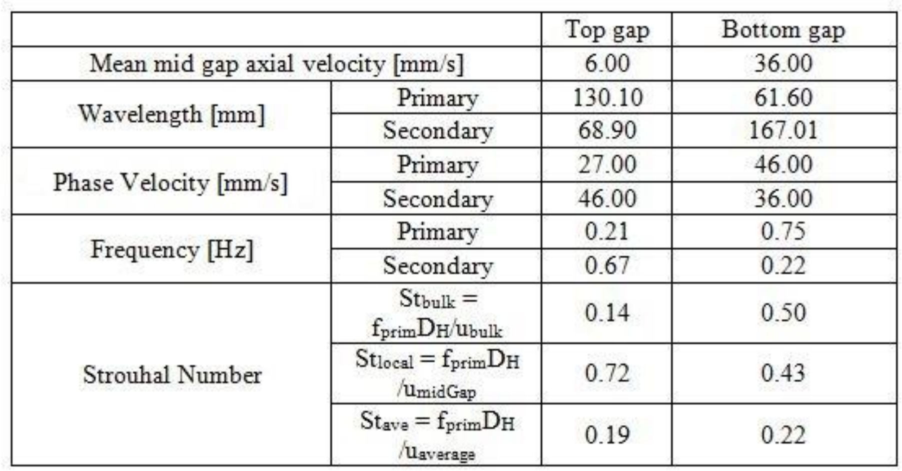

		Top gap	Bottom gap
Mean mid gap axial velocity [mm/s]		6.00	36.00
Wavelength [mm]	Primary	130.10	61.60
	Secondary	68.90	167.01
Phase Velocity [mm/s]	Primary	27.00	46.00
	Secondary	46.00	36.00
Frequency [Hz]	Primary	0.21	0.75
	Secondary	0.67	0.22
Strouhal Number	$St_{bulk} = f_{prim}D_H/u_{bulk}$	0.14	0.50
	$St_{local} = f_{prim}D_H/u_{midGap}$	0.72	0.43
	$St_{ave} = f_{prim}D_H/u_{average}$	0.19	0.22

Table 4.1 Characteristics of the gap pulse trains in early stage at 31.05 seconds.

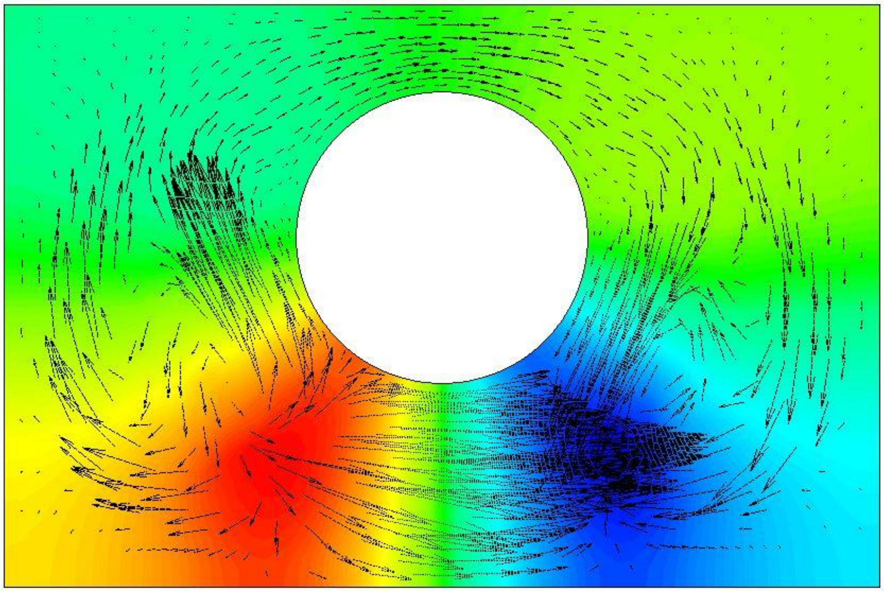

Figure 4.5 Contour plot of pressure on cross section plane at z=0.567m, time is 43.95 seconds. Vectors showing velocity tangential to the plane.

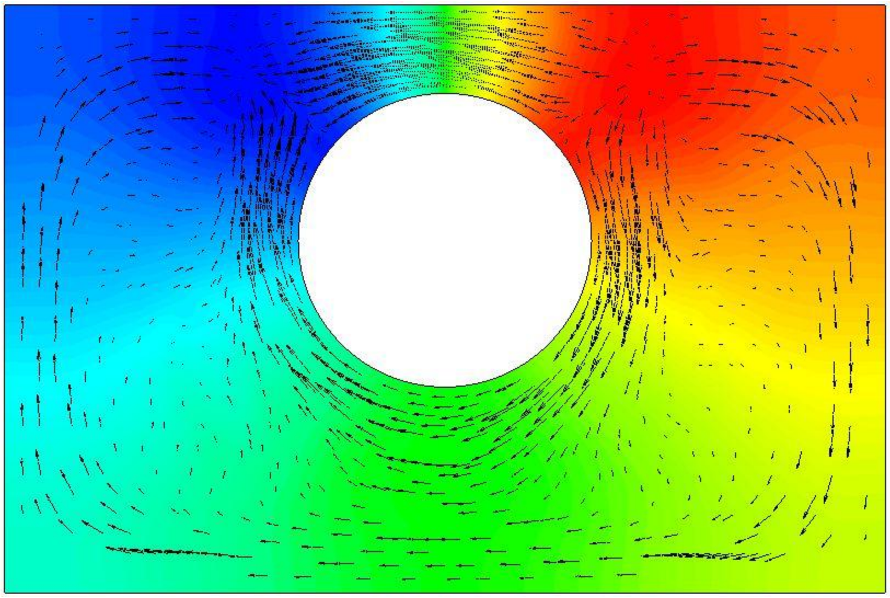

Figure 4.6 Contour plot of pressure on cross section plane at z=0.181m, time is 43.95 seconds. Vectors showing velocity tangential to the plane.

Figure 4.5 and Figure 4.6 show pressure contour plots on cross section planes at z=0.395m and z=0.194m respectively at 43.95 seconds. Figure 4.5 corresponds to a peak in the primary bottom pulse train. In Figure 4.5 the pressure extremes are located in the bottom gap region near the rod edges, associated with the bottom gap flow that dominates the crossplane flow, which can be clearly seen. The much weaker flow in the top gap also appears to be driven by these bottom gap pressure extremes, resulting in the 'echo' flow in the top gap. Figure 4.6 shows a cross section through a peak in the primary top pulse train. In this case, the pressure extreme are located in the top gap region near the rod edges. Pressure extremes here appear to also drive a weaker flow through the bottom gap, causing the bottom secondary pulse train. Driven by the primary gap pressure fields and regions of high axial velocity gradient, the echo secondary pulses are in phase and in the same direction as the primary pulses.

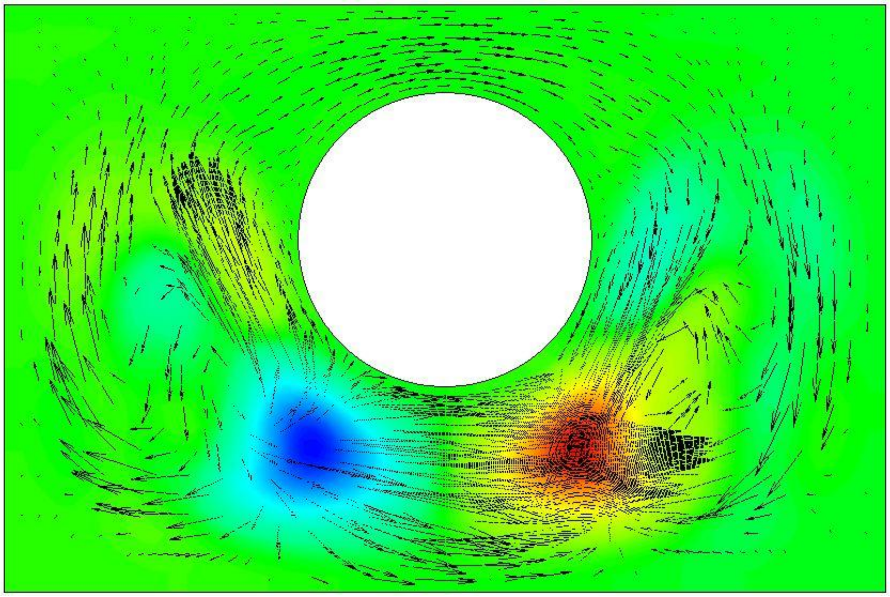

Figure 4.7 Contour plot of axial velocity gradient on cross section plane at z=0.567m, time is 43.95 seconds. Vectors showing velocity tangential to the plane. Red is positive and blue is negative.

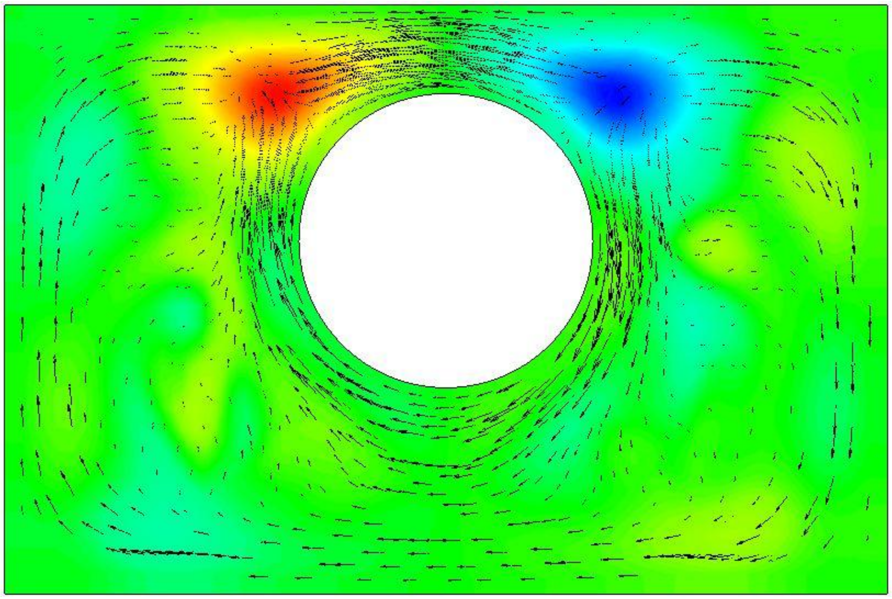

Figure 4.8 Contour plot of axial velocity gradient on cross section plane at z=0.181m, time is 43.95 seconds. Vectors showing velocity tangential to the plane. Red is positive and blue is negative.

Figure 4.7 and Figure 4.8 show the axial velocity gradient on the same aforementioned cross planes. A positive axial velocity gradient creates a sink for spanwise flows whereas negative axial velocity gradient acts as a source of spanwise flows. As expected, in Figure 4.7 where the bottom primary pulse train is peaking the extremes of the axial velocity gradient are located in the bottom gap region near the rod edge. In Figure 4.8, the extremes of the axial velocity gradient are located in the top gap where the primary top pulse train is peaking. The secondary flow or "echoes" of the primary pulse trains in the opposing gap regions can also be seen in these figures.

Fast Fourier Transforms were used to convert spanwise gap velocities from spatial domain into wavenumber domain in order to ascertain the wavelength of the pulse trains. In the early stage of development, the FFT shows two clear peaks for both the top and bottom gap pulse trains. In Figure 4.9 and Figure 4.10, as expected, the peak with the higher magnitude in one gap (the primary) coincides with the peak with the lower magnitude in the other gap (the echo). The peak wavelengths are shown in Table 4.2.

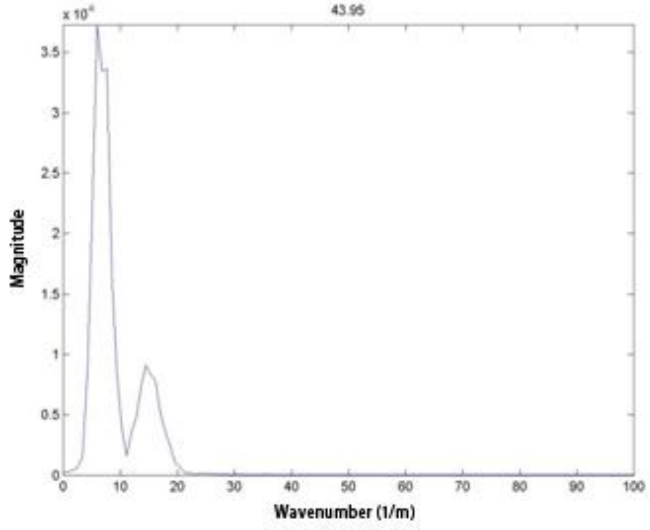

Figure 4.9 Fourier spectrum of cross stream velocities at the mid point of the top gap at 43.95 seconds.

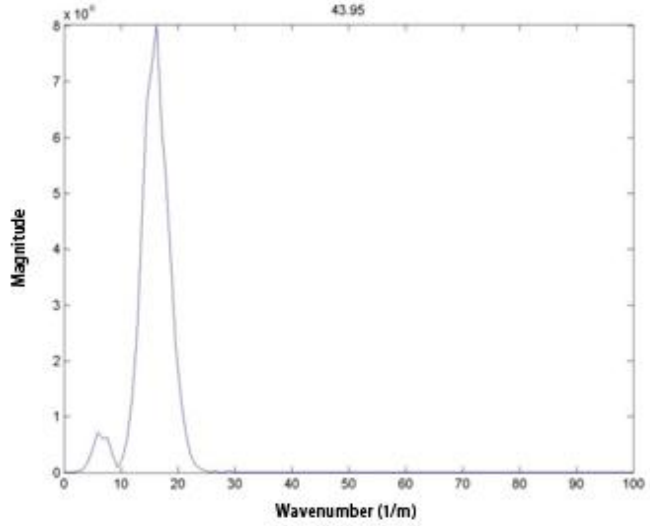

Figure 4.10 Fourier spectrum of cross stream velocities at the mid point of the bottom gap at 43.95 seconds.

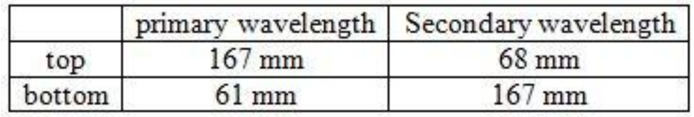

	primary wavelength	Secondary wavelength
top	167 mm	68 mm
bottom	61 mm	167 mm

Table 4.2 Wavelength of top and bottom gap pulse trains at 43.95 seconds.

In each gap, the primary pulse train and the secondary pulse train have different phase velocities, which results in interactions between the primary and secondary pulse trains. At this early stage, as the faster moving pulse train passes through the slower moving pulse train, their wavelength, frequency and velocity remain distinctly separate while locally the spanwise velocity is a superposition of the magnitudes of the two pulse trains. This sequence of pulse train growth and interaction, which is separate and as the superposition of independently developing top and bottom gap flows, can be seen in Figure 4.11 and in Figure 4.4.

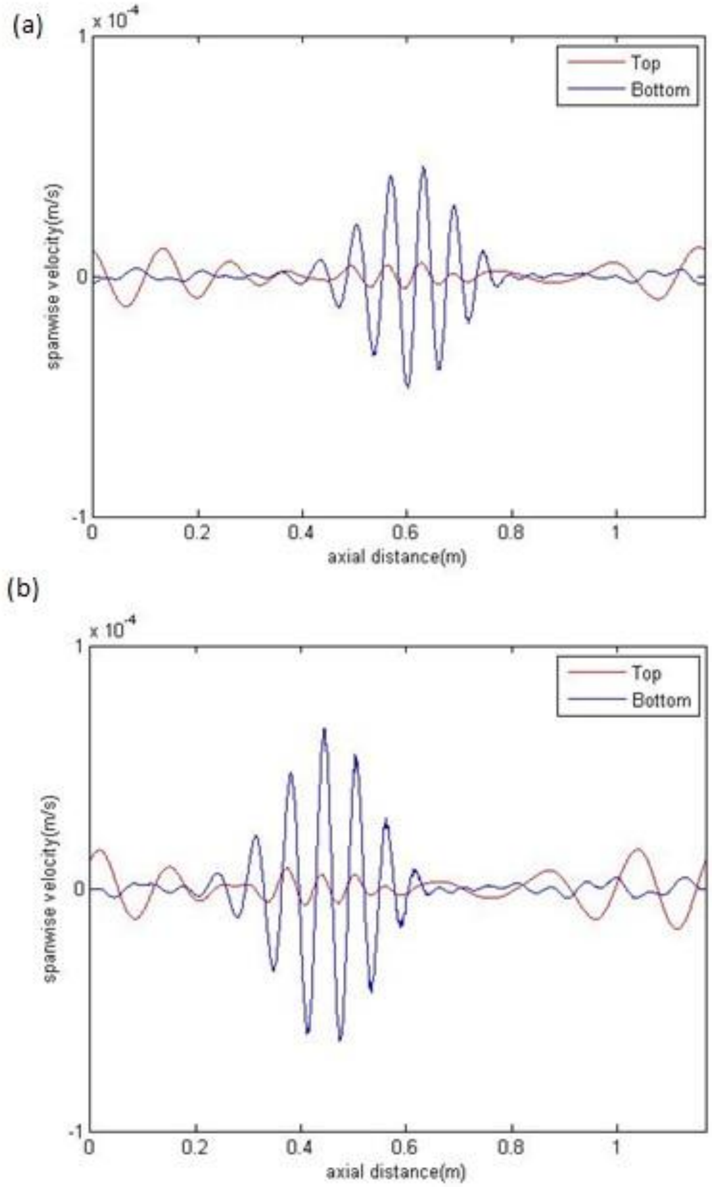

Figure 4.11 Spanwise velocities of top and bottom gap centerlines. Flow goes from right to left. (a) t = 43.95 seconds (b) t = 49 seconds

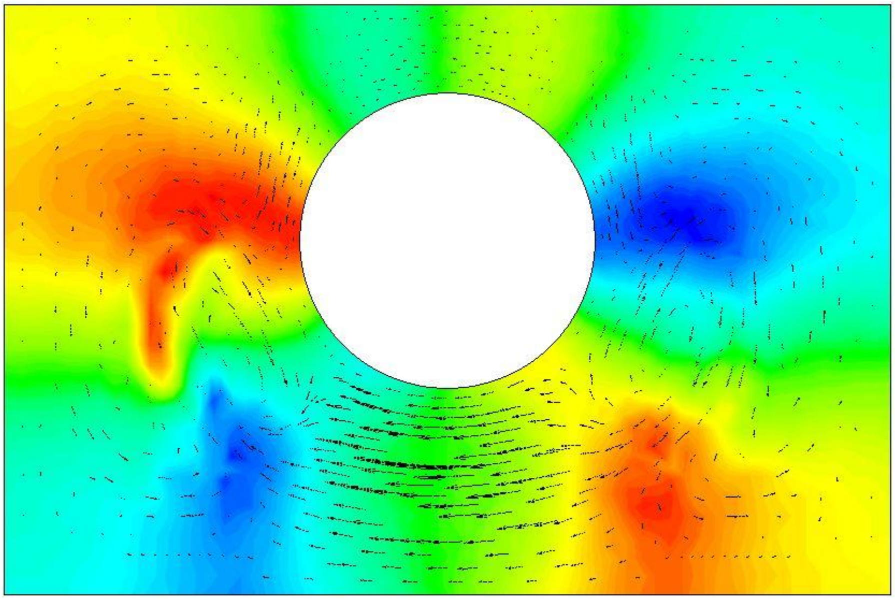

Figure 4.12 Contour plot of pressure on cross section plane at z=0.276m, time is 48 seconds. Vectors showing velocity tangential to the plane.

Figure 4.12 shows the pressure field on a cross section at a time in between those of Figure 4.11 and a location where bottom gap pulse trains are about to start encountering the top gap pulse train. The two pairs of pressure extremes associated with both the top and bottom gaps can be clearly seen. These pressure extremes are out of phase here, so that while the bottom gap flow remains relatively strong the 'echo' flow in the top gap has been essentially suppressed.

4.3 Later Stage Development

As opposed to the early stage where spanwise velocities are higher in the bottom gap, at about 120 seconds the spanwise velocities in the top gap start to outgrow the spanwise velocities in the bottom gap (Figure 4.2). This is the onset of the later stage of the progression.

At this stage, the length of the top pulse train has grown to nearly fill the computational domain while that of the bottom pulse train is still only about half of the computational domain. A contour plot of the spanwise velocities in the top and bottom gaps can be seen in Figure 4.13 with the velocity profile in Figure 4.14 and wavenumber spectrum in Figure 4.15 and Figure 4.16.

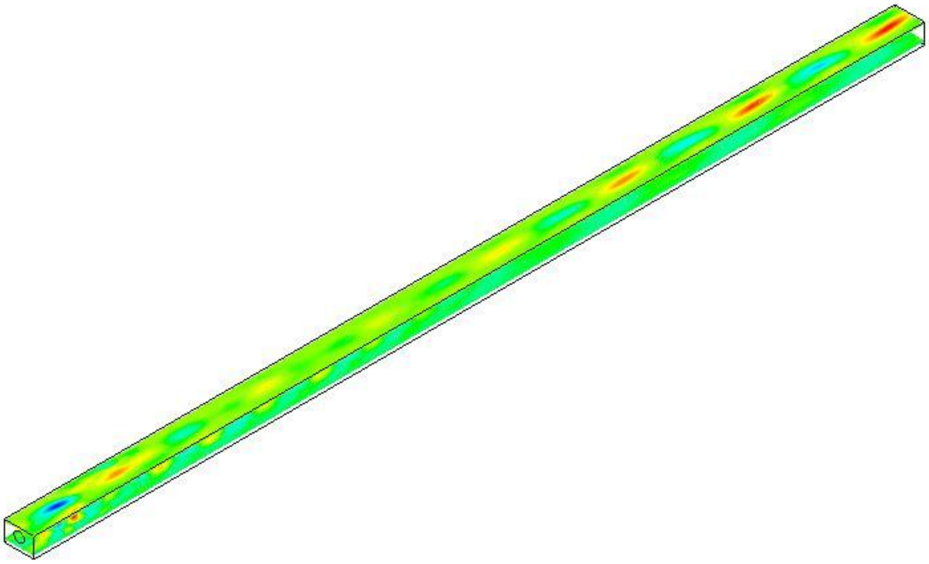

Figure 4.13 Contour plot of spanwise velocities in the top and bottom gap regions at 120 seconds.

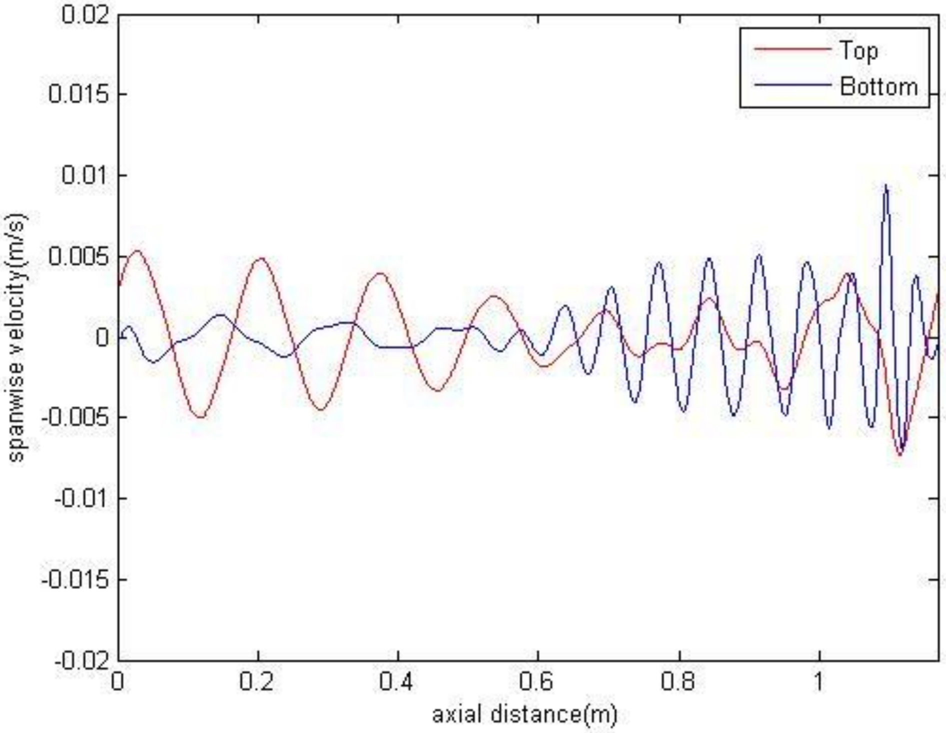

Figure 4.14 Spanwise velocities in the top and bottom gap regions at 120 seconds.

The interaction of the primary and secondary pulse trains causes the pulse trains in each gap start to lose their distinct identity after approximately 120 seconds. As can be seen in Figure 4.14 and Figure 4.16, smaller structures began to form in the bottom gap resulting in a third peak with higher wavenumber than the previous peaks. These smaller structures have their “echo” in the top gap but with much smaller magnitude as can be seen in Figure 4.15.

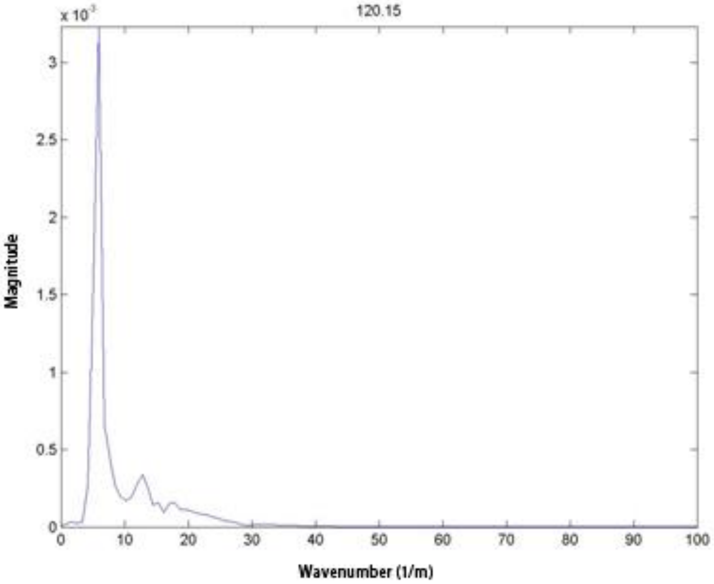

Figure 4.15 Fourier spectrum of cross stream velocities at the mid point of the top gap at 120.15 seconds .

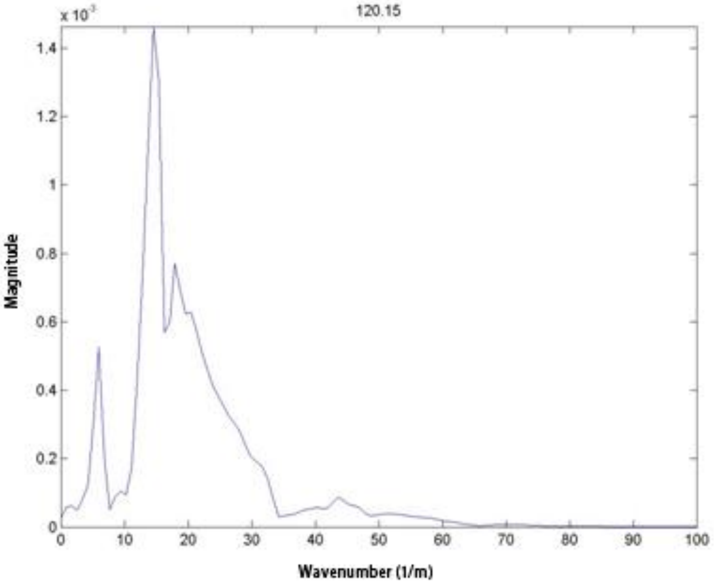

Figure 4.16 Fourier spectrum of cross stream velocities at the mid point of the bottom gap at 120.15 seconds.

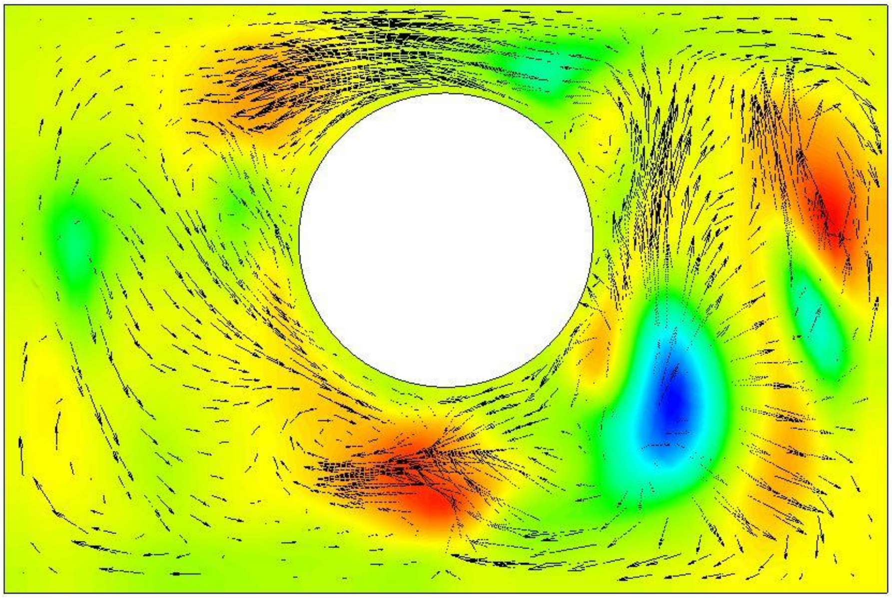

Figure 4.17 Contour plot of axial velocity gradient on cross section plane at z=0.111m, time is 120.15 seconds. Vectors showing velocity tangential to the plane. Red is positive and blue is negative.

Figure 4.17 shows a contour plot of axial velocity gradient on a cross section plane where the top gap velocity pulsations are large and distinct at 120.15 seconds. The flow in the rest of the cross section shows considerable complexity as compared to earlier times of Figure 4.8 for example. As opposed to having distinctive axial velocity gradient extremes at either the bottom or top gap in the case of early stages, axial velocity gradient extremes are located at both the top and bottom gap regions and show notable asymmetry.

As the pulse trains continued to grow, the primary pulse train in the bottom gap started to dissipate into smaller structures in terms of wavelengths. The secondary pulse train the bottom gap eventually outgrows the primary pulse train and becomes the main structure in the bottom gap. Figure 4.18 shows the time where the primary and secondary pulse trains in the bottom gap have the same magnitudes. Right after this time, the dominant structures in the bottom gap takes the frequency and magnitude of the secondary pulse train, which is also the frequency and wavelength of the primary pulse train in the top gap.

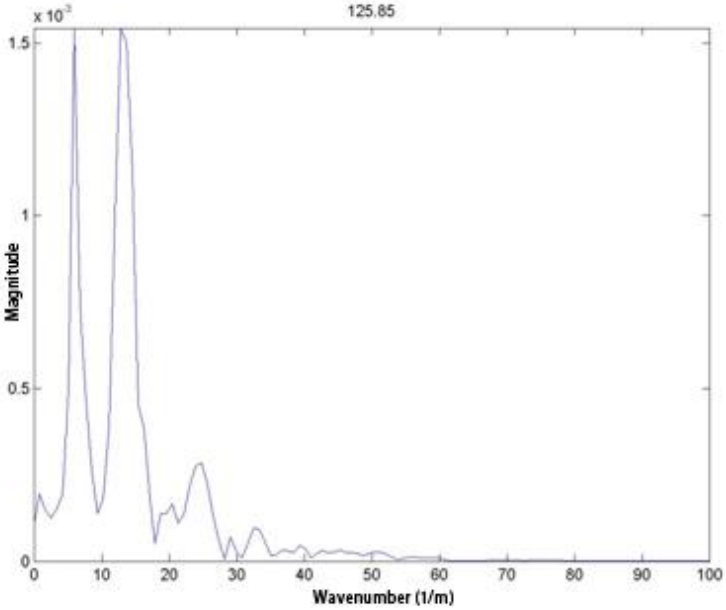

Figure 4.18 Fourier spectrum of cross stream velocities at the mid point of the bottom gap at 125.85 seconds showing the primary and secondary pulse trains having the same magnitudes.

With the primary pulse train in bottom gap diminishing, its echo, the secondary pulse train in top gap becomes even more insignificant. The net effect is flow in both gaps becomes dominated by the primary top gap pulse train. The top and bottom pulse trains now share the same characteristics with similar wavelength, but with different phase angles as can be seen in Figure 4.19 and Figure 4.20. The entire domain of top and bottom gap regions is now occupied by pulse trains that are no longer independent of each other. At this stage, the bottom pulse train lags the top by approximately one third of a wavelength which is identified by shifting the signal of the top pulse in space in the axial direction. The shifted distance corresponding to the highest sample correlation coefficient is 0.06 m which is about 60 degrees in phase angle.

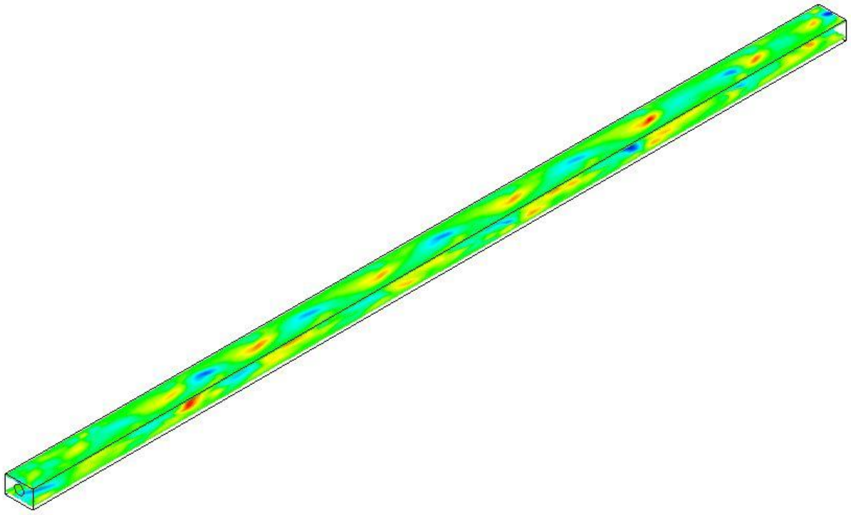

Figure 4.19 Contour plot of spanwise velocities in the top and bottom gap regions at 151.9 seconds.

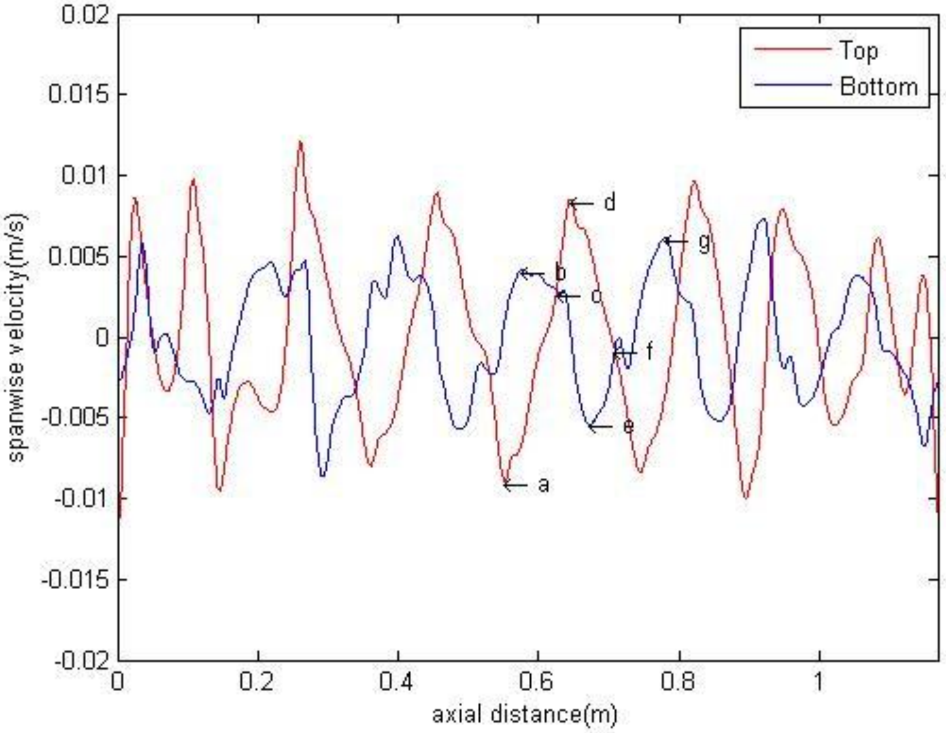

Figure 4.20 Spanwise velocities of top and bottom gap pulse trains at 151.9 seconds showing similar wavelength.

Figure 4.21 is a sequence of contour plots of axial velocity gradient with vectors representing cross plane velocity at 151.9 seconds. The location of the cross planes are “a” through “g” on Figure 4.20 respectively. The sequence starts at peak in the top gap flow pulsation, where the axial velocity gradient extremes are on either side of the top gap. The top gap flow is the dominant feature and little flow is observed in the rest of the cross section.

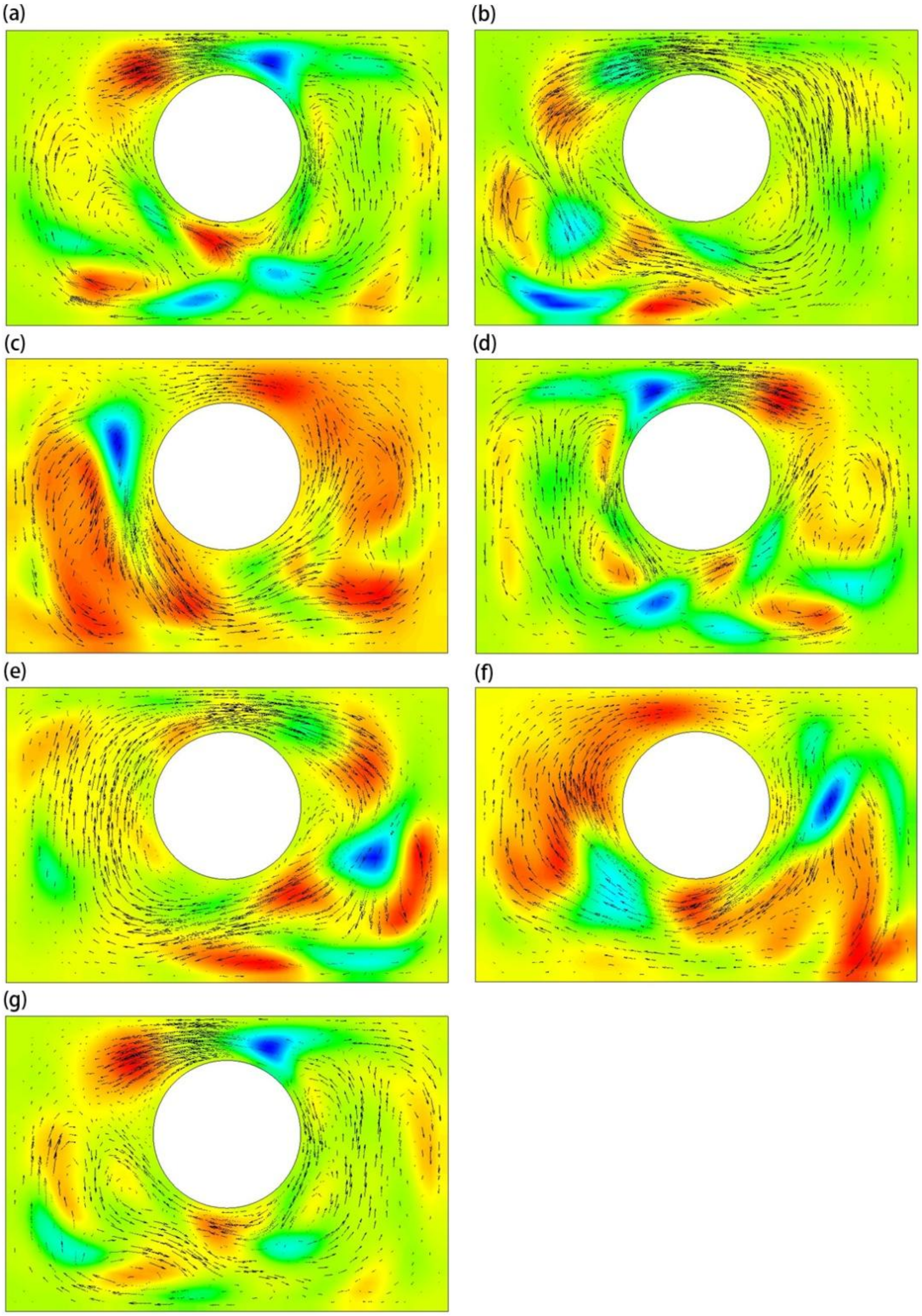

Figure 4.21 Contour plot of axial velocity gradient at 151.9 seconds. Cross section plane locations refer to Figure 4.20. Vectors showing velocity tangential to the plane. Red is positive and blue is negative.

Figure 4.21 (a) shows the cross plane at location “a” which is at a local crest of the top spanwise velocity. Axial velocity gradient extremes are located in the top gap near the edge of the rod. The magnitude of the bottom spanwise velocity is small.

Figure 4.21 (b) shows the cross plane at location “b” which is at a local peak of bottom spanwise velocity. Unlike in Figure 4.21 (a), the bottom gap flow now has a uniform source and sink, resulting in a larger spanwise velocity.

Figure 4.21 (c) shows the cross plane at location “c”. Top and bottom pulse train have the same spanwise velocity at this time and location. Unlike at the locations of spanwise velocity peaks and crests where axial velocity gradient extreme are more concentrated in smaller areas, in this case they are more spread out hence smaller driving force for spanwise flow.

Figure 4.21 (d) shows the cross plane at location “d” which is at a local peak of top spanwise velocity. The distribution of axial velocity gradient in a reversed mirror image of that in Figure 4.21 (a), as the spanwise velocity is at its local maximum only with its sign reversed.

Figure 4.21 (e) shows the cross plane at location “e” which is at a local crest of bottom spanwise velocity. The distribution of axial velocity gradient in a reversed mirror image of that in Figure 4.21 (b), as the spanwise velocity is at its local maximum only with its sign reversed.

Figure 4.21 (f) shows the cross plane at location “f”. Top and bottom pulse train have the same spanwise velocity at this time and location. Similar to Figure 4.21 (c) the extreme of axial velocity gradient is less concentrated than that in other figures.

Figure 4.21 (g) shows the cross plane at location “g” which is at a local crest of top spanwise velocity. The velocity profile has come to a full period and the axial velocity gradient in this case is a repeat of that in Figure 4.21 (a).

The development of the interaction between the two gaps can also be illustrated by tracking fluid particles released from the center of the top gap, details of which are given in the next section. Figure 4.22 and Figure 4.23 show the time veolution of the spanwise and vertical positions respectively of particles released from the centre of the top gap. In the early stages the extreme of axial velocity gradient were located inside the gap regions both for the top or the bottom gaps, but the spanwise velocity magnitudes were not large enough for the fluid to traverse outside of the gap region. Spanwise movements of the fluid were confined within the gap regions. As the pulse trains individually grow in magnitude, the spanwise velocities eventually becomes large enough for fluid to be convected to the outside of the gap regions as can be seen in Figure 4.22. In the early stages of pulsation development the particle traces were confined in the gap regions which were represented by the dashed lines. The particles stayed in the top gap region until about 120 seconds, which marked the start of the late stage of the growth. As a result of fluid entering opposite gap regions, smaller structures began to form which led to both gaps being dominated by bigger wavelength. After 120s, the increased spanwise displacement of the fluid into the subchannels allows it to be transported vertically by flows throughout the domain. The fluid particles paths then become much larger and include complete circulations around the rod.

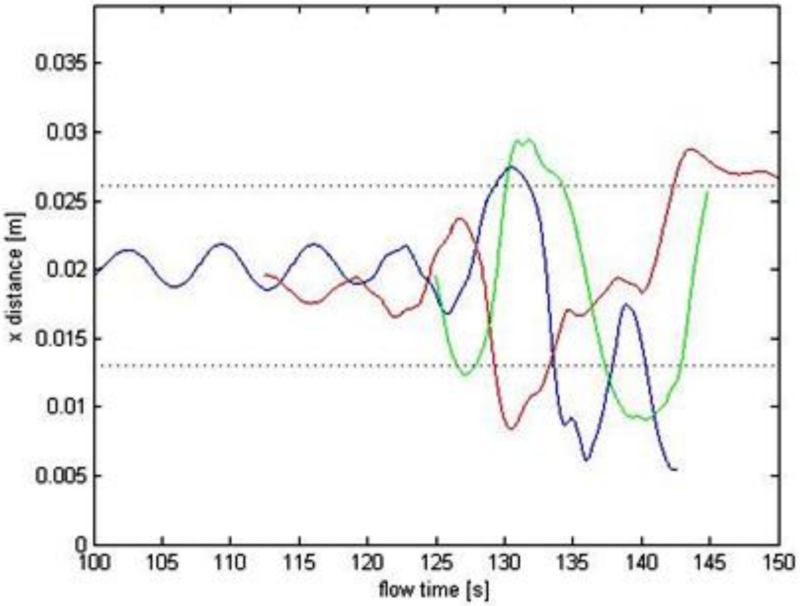

Figure 4.22 cross steam distance of particle trace showing three different particles in flow time. Dashed lines are the left and right edge of the rod. Particles were released at the center of the top gap.

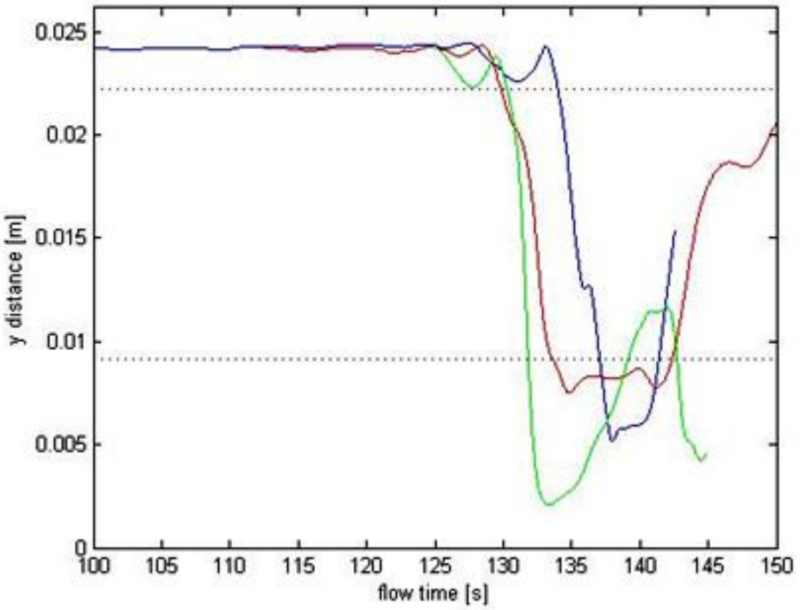

Figure 4.23 vertical distance of particle trace showing three different particles in flow time. Dashed lines are the top and bottom edge of the rod. Particles were released at the center of the top gap.

4.4 Summary of the Growth Stages

The simulation started with a purely axial flow. The inflection points in the velocity profiles caused by difference in flow resistance give rise to instability in the flow and independent pulse trains start to form in the top and bottom gap regions. Pressure coupling at the cross plane leads to "echoes" of the pulse trains in the opposite gap region. As a result, one primary pulse train and one secondary pulse train exist in each of the gap region. The primary pulse train and secondary pulse train have different wavelengths and phase velocities. In the early stage where the spanwise velocity are small in magnitude, the primary pulse train and secondary pulse train do not interact when passing through each other. When they collide, they retain their individual wavelength and phase velocity. The local spanwise velocity is a simple superposition of the two colliding pulse trains. At the later growth stage starting around 120 seconds, spanwise velocities and cross gap velocities became large enough that fluid particles in the gap region can be convected into opposing gap region. As a result the primary and secondary pulse train in each gap started to become interact after they collide with each other, making both gaps share similar frequencies and wavelengths.

4.5 Lagrangian Based Analysis

In the experiments of Gosset and Tavoularis [3], neutral buoyancy dye particles were released at a single injection point in the middle of the top gap. This injection point was 0.57 domain length downstream of the inlet and was deemed far enough from the downstream that entrance effects could be neglected. Single time photographs of the resulting fluid/dye particle trajectory streaklines were then used to determine the wavelength of the cross-stream flow pulsations by measuring the distance between zero-crossings of the dye traces. With this wavelength, frequencies and Strouhal numbers of the oscillations were then determined.

As part of validation of the numerical simulation, and also to help understand the flow, similar Lagrangian trajectories were obtained from the CFD results using massless fluid particles injected into the flow at a single mid-gap location.

Figure 4.24 shows a dye streak image from experiments [3] alongside a particle streak line from numerical simulation. Both images show similarly-sized hairpin shape traces, providing a good qualitative comparison with the experimental results. An explanation of how such hairpin shapes can form is included at the end of the next section.

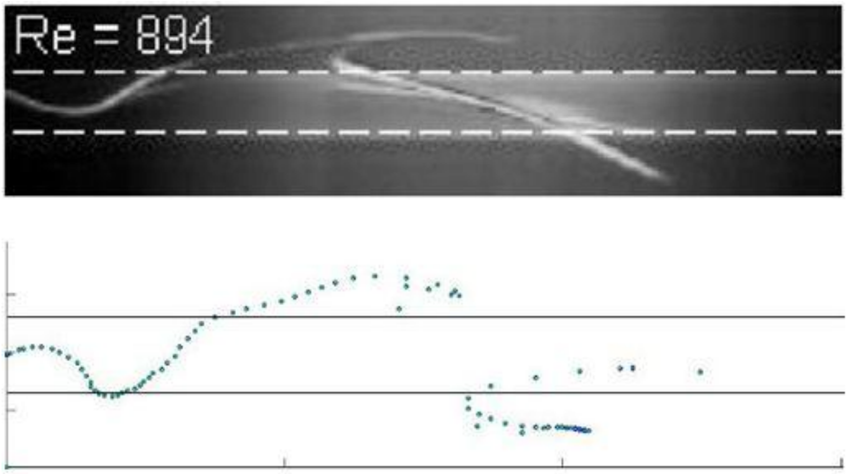

Figure 4.24 Comparison of dye streak from experiments to particle streak from simulation. Dye streak image from Gosset and Tavoularis [3].

Two other typical particle streaklines are shown in Figure 4.25 that show the downstream transport and development of a tracer streakline.. It can be seen that the distance to the first zero-crossing grows over the half the period of the spanwise flow oscillations, but also that the fully grown zero-crossing distances can be highly variable.

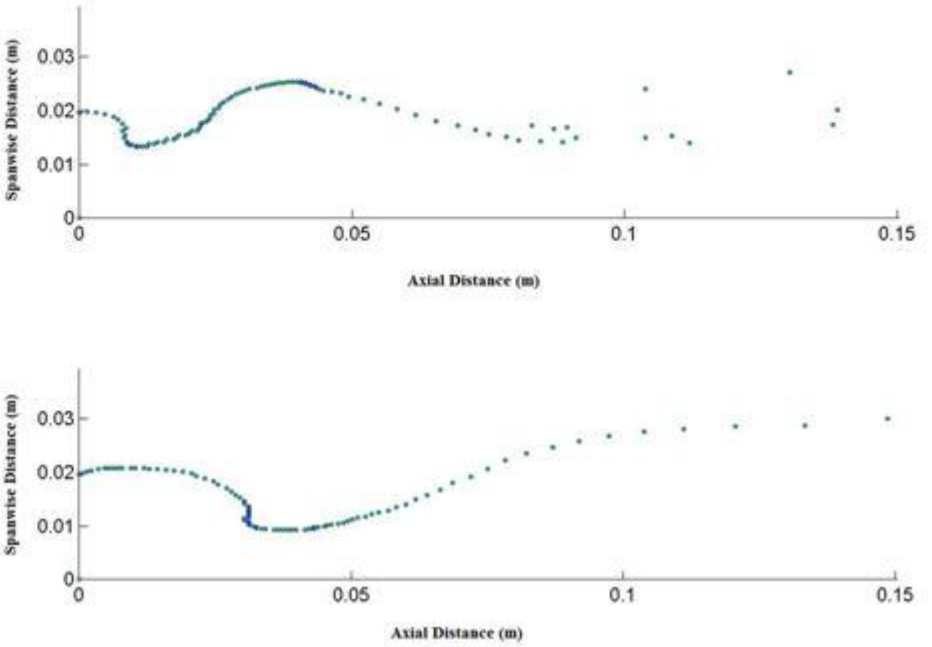

Figure 4.25 Particle streaklines in top gap for Re=900 at 208.08 seconds (top) and 212.04 seconds (bottom). The traces shown are the result of particles released every 0.03 seconds. The mid gap release point is at a spanwise distance of 0.02m.

There are a number of issues with using such a Lagrangian trajectory-based approach to make direct comparisons between the experimental and the CFD results. There is an obvious difficulty in determining zero-crossings in such traces that have complex shapes and are not always symmetric about the rod centerline. An analytical model was then created with Lagrangian tracking of massless fluid particles through a simplified presumed velocity field to examine some of these issues. In this analysis, the cross-stream velocity $v_x(z,t)$ is considered to be as a traveling plane wave so that:

$$v_x(z,t) = A(x)\cos\left[\frac{2\pi}{\lambda}(z-ct)+\phi\right]$$

Equation 4.1

where λ is the wavelength, c is the wave velocity, and ϕ is a phase shift. The amplitude of the oscillating velocity A is here simply treated as a constant so that $v_x(z,t)$ is not a function of x. An axial velocity $v_z(x)$ is simply considered to be a uniform axial flow v_{zMAX} with a momentum deficit in the gap region

$$v_z(x) = v_{zMAX} - (v_{zMAX} - v_{zMIN})\exp\left[-\frac{x^2}{x_{ROD}^2}\right]$$

Equation 4.2

where v_{zMIN} is the velocity at the centre of the gap (with a width of x_{ROD}). The main parameters of the model roughly match those in Table 4.1: $A = 5$ *mm/s*, $\lambda = 160$ *mm*, c = 27mm/s, v_{zMIN} = 6 mm/s, v_{zMAX} = 23 mm/s, x_{ROD} = 10 mm.

With a uniform axial flow (i.e. $v_{zMIN} = v_{zMAX}$), the axial position of a tracer particle is simply a proxy for the time elapsed since its injection. The individual tracer particles are injected as a set of particles over a time interval. The spanwise position of each tracer particle is usually not symmetric about the rod/injection centerline depending on its release point in the oscillating cross-stream velocity cycle. For instance, if the release time coincides with a zero in the spanwise velocity cycle, the particle will spend the entire first half of the cycle being transported away from the centerline, then the second half returning to the centerline. A zero crossing time would then be a full period of the cycle. In contrast, if the release time is just before a max or min of the velocity cycle, the tracer will only move a very short distance away from the centerline before the returning and zero-crossing. When a set of particles are released over an entire cycle (and examined at a single time snap-shot), a streakline with a wavelength λ is produced. The streakline is not a simple sinusoid, but has various waveforms and envelope shapes controlled mainly by the difference between the wave velocity c and the axial flow v_z. Consequently, the distance between two consecutive tracer zero-crossings does not give half the wavelength λ.

With a non-uniform axial velocity, the tracer streaklines show considerably more complexity (Figure 4.26). The reduced axial displacement of the tracers in the gap region exposes them to different phases of the time and space varying cross-stream velocity. Prolonged residence within a cross-flow velocities can drive the particles out of the gap where they then experience larger axial displacements compared to particles retained within the axially slower gap. Later particle releases can then overtake earlier releases forming the hairpin shapes in the streaklines seen previously (Figure 4.24). The variation in axial velocity also consistently produces zero-crossing intervals that are shorter than half the wavelength of the underlying cross-stream velocity fluctuations.

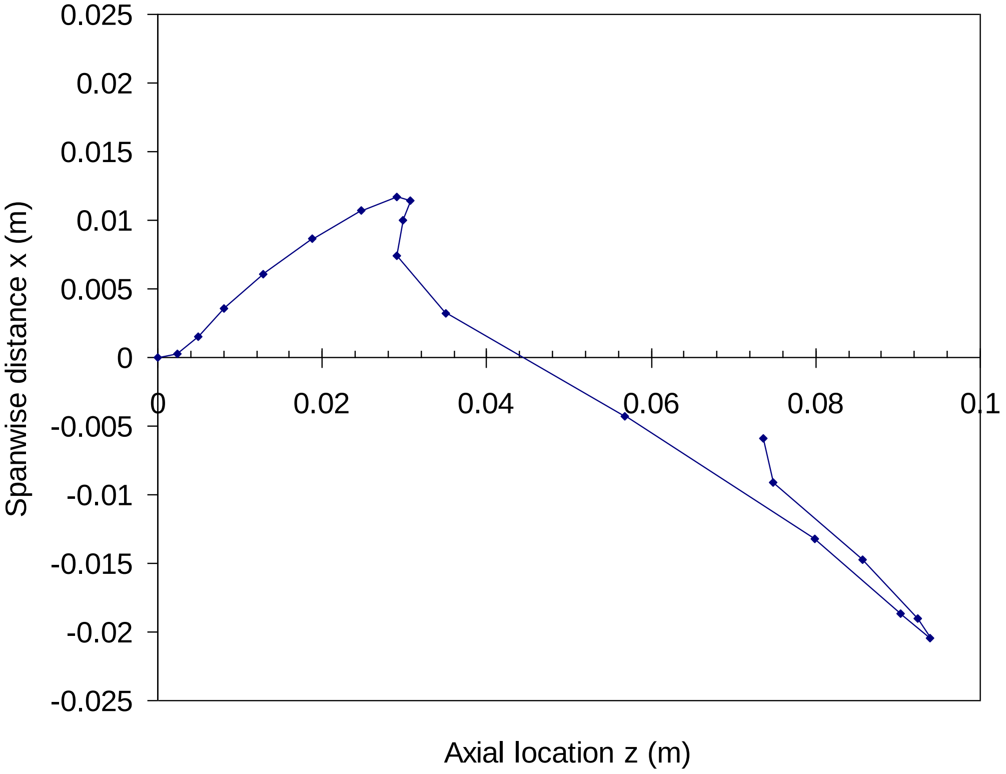

Figure 4.26 Sample streakline trace from the presumed velocity field. The main parameters of the model roughly match those in Table 4.1: $A = 5$ mm/s, $\lambda = 160$ mm, c = 27mm/s, v_{zMIN} = 6 mm/s, v_{zMAX} = 23 mm/s, x_{ROD} = 10 mm. Particles are released every 0.4 s, and the line joining the particles is simply to aid in showing the order of particle release.

More complexity could be built into this analytical model, in particular, the amplitude of the travelling plane wave of the spanwise fluctuations (*A*) could be expressed as a function of the spanwise direction in a manner such as:

$$A(x) = A_0 \exp\left[-\frac{x^2}{x_{ROD}^2}\right]$$

Equation 4.3

This would more accurately represent the spanwise extent of the spanwise pulsations as seen in sections 4.1-4.4, and limited the spanwise transport of the tracer particles. Similarly, the spanwise oscillations could be represented as wave packets (with a limited streamwise extent), rather than as a traveling plane wave - this would better represent the development stages of the pulsations, but would be of limited value in comparing with the experimental values. Adding these additional features to the analytical model was not done as the model is still limited by the presumed nature of the velocity field; in reality, the spanwise fluctuations transport axial momentum (higher speed fluid into the gap, and lower speed fluid out of the gap) along with the tracers, as was seen in the detailed CFD results. However, the analytical model, as is, does still demonstrate how the experimentally seen tracer streaklines do not give a true measure of the wavelength and frequency of the spanwise velocity fluctuations.

In spite of these difficulties, using zero-crossing based wavelengths and frequencies from the present CFD results will allow some comparison with the experimental results of Gosset and Tavoularis [3]. From massless tracer particle releases in the CFD results, the time interval τ is defined as the travel time of the particle in a streakline that first returns to the spanwise centerline (i.e. the time taken for the streakline to zero-cross). The axially downstream distance of this zero-crossing is also recorded. The maximum zero-crossing time intervals and distances would then be the match of Gossett and Tavoularis' half period and half wavelength visual observations; although, as noted before, these are not true measures of the cross-stream velocity oscillation period and wavelength. Plots of zero-crossing time interval τ and distance are shown in Figure 4.27 and Figure 4.28 as functions of snapshot time, and the maximums of each cycle obtained.

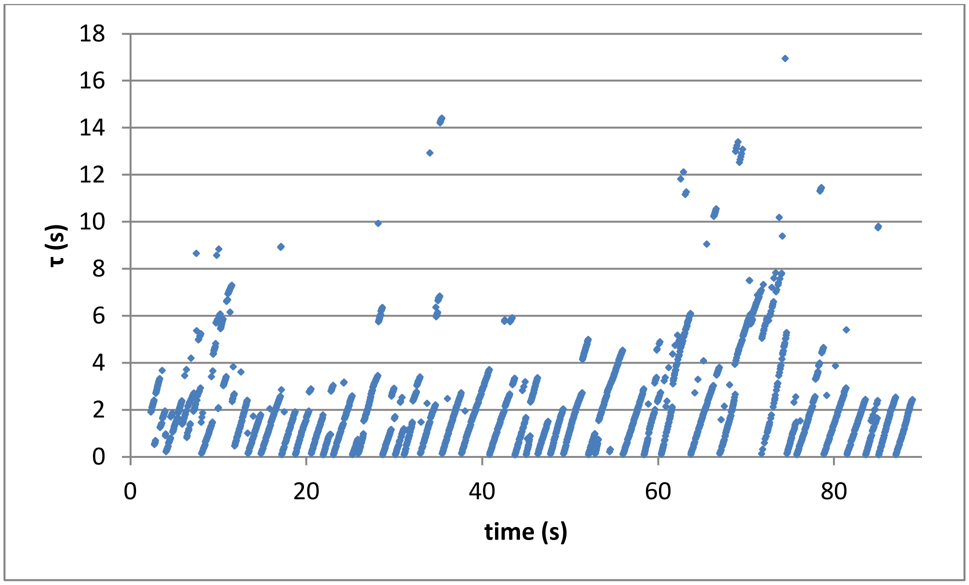

Figure 4.27 τ-time plot for Re=900.

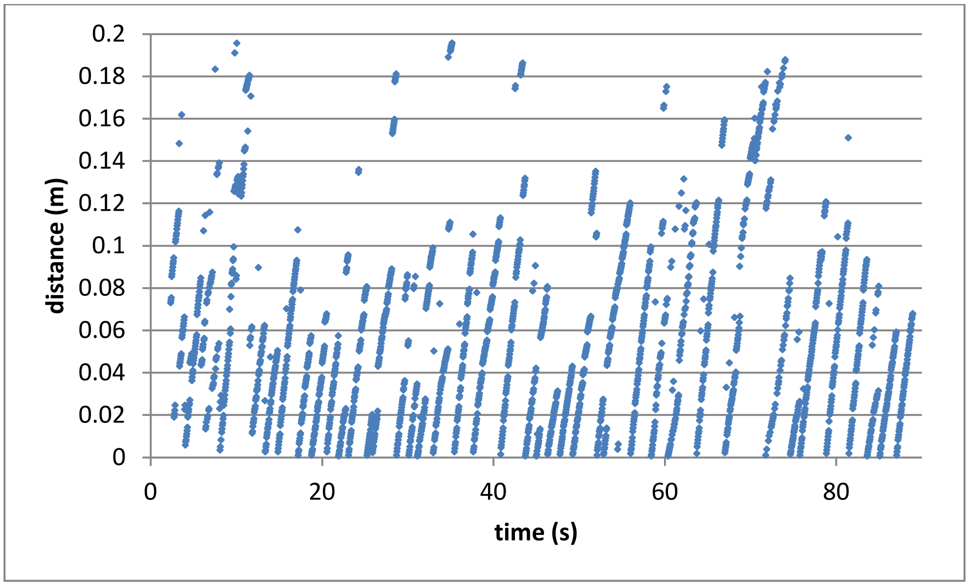

Figure 4.28 Distance-time plot for Re=900.

The average maximum zero-crossing distance obtained from the data shown in Figure 4.28 is about 0.062m corresponding to half the presumed wavelength (then 0.125m or 9.5D). This value of wavelength is much closer to the 5.5D value seen by Gosset and Tavoularis [3] than wavelengths based on an Eulerian cross-stream velocity frequency and some sort of axial velocity (as Chettle's 25D values [5]). A histogram of the wavelengths (non-dimensionalized with the rod diameter D) is shown in Figure 4.29. It can be seen that while the vast majority of the wavelengths are in the range of 0-30D, there is a separate population at about 70D. It is hypothesized here that these larger wavelengths correspond to maximum zero-crossings related to a full (rather than half) wavelengths (likely from cross-stream displacement of the streaklines so they "miss" their zero-crossing), and that these streakline zero-crossings were likely ignored by [3]. If this population is omitted here, the average wavelength would drop from 9.5D to values more similar to that seen by Gosset and Tavoularis [3]. This procedure was repeated for the CFD results at Re= 718 and Re=955, and the resulting wavelengths shown in Figure 4.30 in comparison with Gosset and Tavoularis [3] and Chettle [5], and although as discussed the values differ, there remains the comparable lack of variation of the wavelength with Reynolds number.

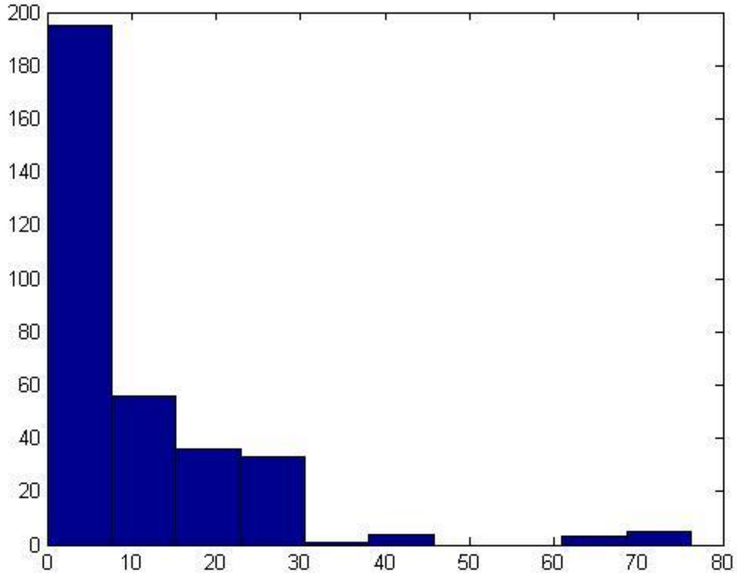

Figure 4.29 Histogram of normalized wavelength for Re=900.

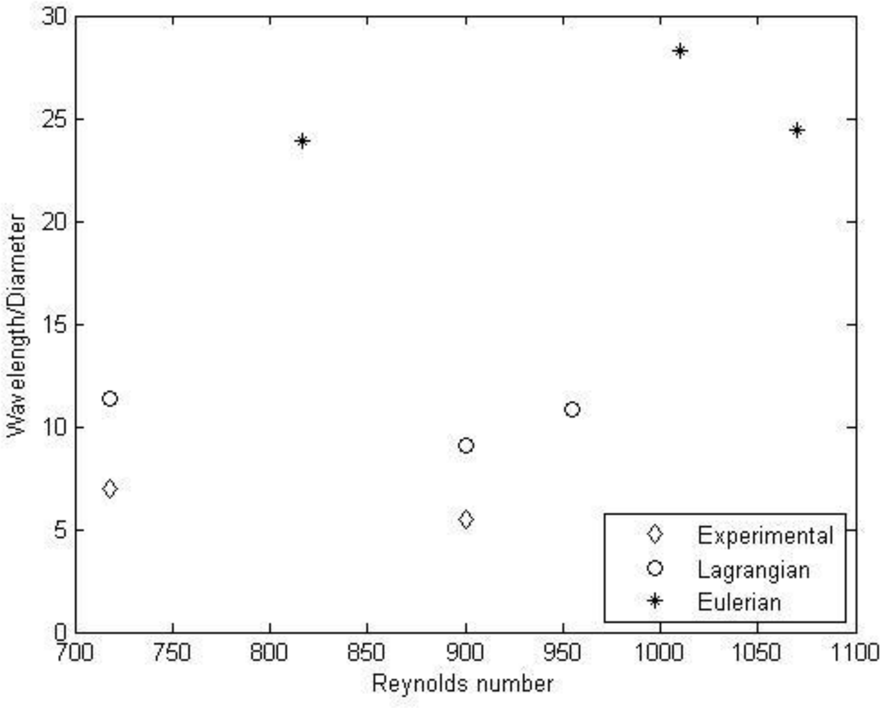

Figure 4.30 Variation of wavelength/diameter with Reynolds number for δ /D=0.3. Experimental data from Gosset and Tavoularis [3]. Eulerian data from Chettle [5].

An analogous procedure was used to obtain the frequencies from the zero-crossing time intervals. An average value of 0.29Hz, corresponding to a Strouhal number of 0.087, was found, similar to the values found by Chettle's Eulerian analysis [5], but roughly 20% higher than that found by Gosset and Tavoularis [3]. The procedure was repeated for Re=718 and Re=955 (Figure 4.31), and the same trends seen at these Reynolds numbers. Another set of frequencies was obtained by discarding the local maximum τ less than 10% of the average local maximums. This gives a frequency of 0.21 Hz and St=0.064. These values are also plotted in Figure 4.31 and are again close to, but roughly 25% less than, that seen by Gosset and Tavoularis [3].

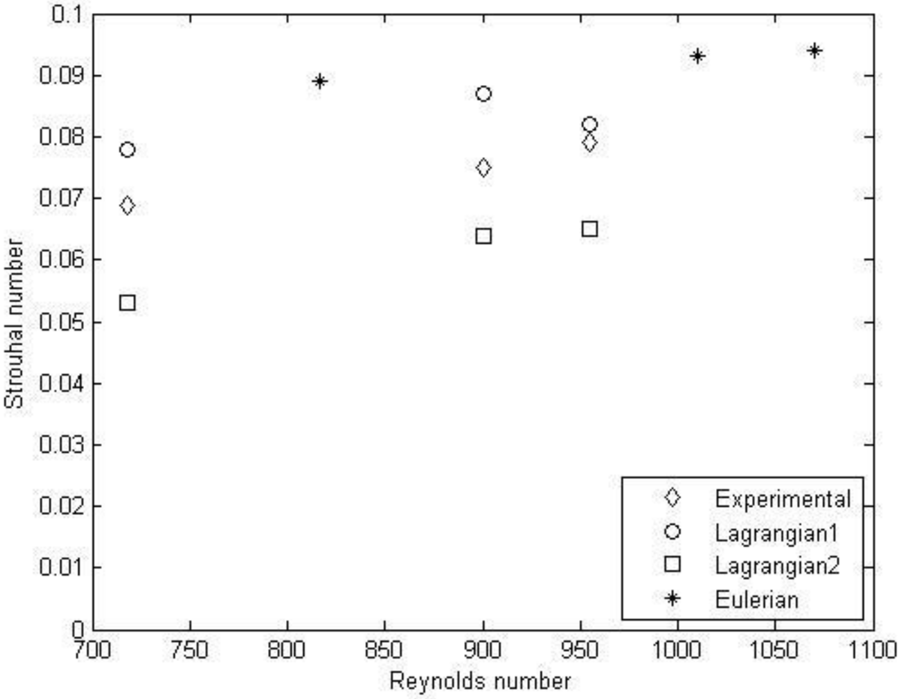

Figure 4.31 Variation of Strouhal number with Reynolds number for δ /D=0.3. Experimental data from Gosset and Tavoularis [3]. Eulerian data from Chettle [5].

Chapter 5 Conclusions

5.1 Summary

This thesis represents, to the author's knowledge, the first study on evolution of intersubchannel pulsating flows. Computational fluid dynamics (CFD) simulations were performed on a simplified geometry consisting of a rectangular duct containing an asymmetrically placed rod. This geometry simulates two gaps with different sizes on the top and bottom of the rod and was motivated by the experimental work of Gosset and Tavoularis [3]. The simulated flows were laminar and quasi-periodic structures were observed. The observations and analysis led to the following conclusions:

1. Instability from inflection in the velocity profile leads to the formation of trains of quasi-periodic structures in both the top and bottom gaps independently. Initially only part of the domain was occupied by these pulse trains.
2. The two pulse trains have different frequencies, wavelengths and phase velocities. Each pulse train has an echo in the opposing gap sharing the same frequency, wavelength and phase velocity but with significantly smaller magnitude.
3. The primary pulse trains associated with the pressure field in each gap and the associated secondary pulsations in the opposite gap move

independently inside each gap. When the primary and echo secondary pulse trains interact with each other, the local spanwise velocity is initially the superposition of the original and echo secondary pulse train. In early stages the original and echo secondary pulse trains retain their independent characteristics of flow development after interacting with each other.

4. In later stages, the formation of the smaller structures in the bottom gap disrupts the primary bottom pulse train and the echo secondary pulse train in the bottom gap then becomes the dominate wave form. This leads to similar characteristics of the structures at the bottom and top gap which are dominated by a single wavelength with additional weakened scales predominantly in the bottom gap.

5.2 Recommendations for Future Work

The present study reported results of flow pulsation development in laminar subchannel flows. It would be beneficial to extend the same study to high Reynolds number turbulent flows typical of the real flows in nuclear reactors. This would be particularly important in CANDU geometries as there is a limited development length determined by the size of the fuel bundle. More complex geometries should also be investigated with respect to interactions between more gaps and channels. The complexity of the gap flow interactions between just two gaps suggests that there will be multiple complex interactions in the fuel bundle with their range of gap widths in connected subchannels.

Bibliography

[1] CANDU, "About Candu," CNADU, [Online]. Available: http://www.candu.com/en/home/aboutcandu/default.aspx. [Accessed 12 11 2015].

[2] J. D. Hooper and K. Rehme, "Large-scale structural effects in developed turbulent flow through closely-spaced rod arrays," *Journal of Fluid Mechanics*, vol. 145, pp. 305-337, 1984.

[3] A. Gosset and S. Tavoularis, "Laminar flow instability in rectangular channel with a cylindrical core," *Physics of Fluids,* vol. 18, no. 4, p. 044108, 2006.

[4] L. Meyer and K. Rehme, "Large-scale turbulence phenomena in compound rectangular channels," *Experimental Thermal and Fluid Science,* vol. 8, no. 4, pp. 286-304, 1994.

[5] A. Chettle, Laminar Simulation of Flow Pulsations in Simplified Subchannel Geometries, M.A.Sc thesis: McMaster University, 2011.

[6] CANDU, "EC6 Enhanced CANDU 6 Technical Summary," Mississauga, 2012.

[7] O. S. Eiff and M. F. Lightstone, "On the modeling of single-phase turbulent energy transport in subchannels," in *Proceedings of the Annual Conference - Canadian Nuclear Society*, 1997.

[8] W. Eifler and R. Nijsing, "Experimental investigation of velocity distribution and flow resistance in a triangular arrary of parallel rods," *Nuclear Engineering and Design,* vol. 5, no. 1, pp. 22-42, 1967.

[9] B. H. Ouma and S. Tavoularis, "Flow measurements in rod bundle subchannels with varying rod-wall proximity," *Nuclear Engineering and Design*, vol. 131, no. 2, pp. 193-208, 1991.

[10] M. S. Guellouz and S. Tavoularis, "Heat transfer in rod bundle subchannels with varying rod-wall proximity," *Nuclear Engineering and Design*, vol. 132, no. 3, pp. 351-366, 1992.

[11] Hosokawa, Yamamoto, Okajima and Tomiyama, "Measurements of turbulent flows in a 2x2 rod bundle," *Nuclear Engineering and Design*, vol. 249, pp. 2-13, 2012.

[12] R. Nijsing, W. Eifler, B. Delfau and J. Camposilvan, "Studies on fluid mixing between subchannels in a bundle of finned tubes," *Nuclear Engineering and Design*, vol. 5, no. 3, pp. 229-253, 1967.

[13] Rehme, "The structure of turbulent flow through a wall subchannel of a rod bundle," *Nuclear Engineering and Design*, vol. 45, no. 2, pp. 311-323, 1978.

[14] W. Eifler and R. Nijsing, "VELASCO-velocity field in asymmetric rod configuartions," EURATOM, Luxembourg, 1973.

[15] M. Renksizbulut and G. I. Hadaller, "An experimental study of turbulent flow through a square-array rod bundle," *Nuclear Engineering and Design*, vol. 91, no. 1, pp. 41-55, 1986.

[16] S. Wu and K. Rehme, "An experimental investigation on turbulent flow through symmetric wall subchannels of two rod bundles," *Nuclear Techonology*, vol. 89, no. 1, pp. 103-115, 1989.

[17] Hooper, "Developed single phase turbulent flow through a square-pitch rod cluster," *Nuclear Engineering and Design*, vol. 60, no. 3, pp. 365-379, 1980.

[18] V. R. Skinner, A. R. Freeman and H. G. Lyall, "Gas mixing in rod clusters," *International Journal of Heat and Mass Transfer*, vol. 12, no. 3, pp. 265-278, 1969.

[19] Tachibana, Oyama, Akiyama and Kondo, "Measurement of heat transfer coefficient for axial air flow through eccentric annulus and seven-rod cluster," *Journal of Nuclear Science and Technology,* vol. 6, no. 4, pp. 207-214, 1969.

[20] Rowe, Johnson and Knudsen, "Implications concerning rod bundle crossflow mixing based on measurements of turbulent flow structure," *International Journal of Heat and Mass Transfer,* vol. 17, no. 3, pp. 407-419, 1974.

[21] Trupp and Azad, "The structure of turbulent flow in triangular array rod bundles," *Nuclear Engineering and Design,* vol. 32, no. 1, pp. 47-84, 1975.

[22] W. J. Seale, "Measurements and predictions of fully developed turbulent flow in a simulated rod bundle," *Journal of Fluid Mechanics,* vol. 123, pp. 399-423, 1982.

[23] V. Vonka, "Measurement of secondary flow vortices in a rod bundle," *Nuclear Engineering and Design,* vol. 106, no. 2, pp. 191-207, 1988.

[24] V. Vonka, "Turbulent transports by secondary flow vortices in a rod bundle," *Nuclear Engineering and Design,* vol. 106, no. 2, pp. 209-220, 1988.

[25] Seale, "Turbulent diffusion of heat between connected flow passages Part 1," *Nuclear Engineering and Design,* vol. 54, no. 2, pp. 183-195, 1979.

[26] K. Rehme, "Experimental observations of turbulent flow through subchannels of rod bundles," *Experimental Thermal and Fluid Science,* vol. 2, no. 3, pp. 341-349, 1989.

[27] Möller, "On phenomena of turbulent flow through rod bundles," *Experimental Thermal and Fluid Science,* vol. 4, no. 1, pp. 25-35, 1991.

[28] Möller, "Single-phase turbulent mixing in rod bundles," *Experimental Thermal and Fluid Science,* vol. 5, no. 1, pp. 26-33, 1992.

[29] K. Rehme, "The structure of turbulence in rod bundles and the implications on natural mixing between the subchannels," *International Journal of Heat*

and Mass Transfer, vol. 35, no. 2, pp. 567-581, 1992.

[30] X. Wu and A. C. Trupp, "Experimental study on the unusual turbulence intensity distributions in rod-to-wall gap regions," *Experimental Thermal and Fluid Science,* vol. 6, no. 4, pp. 360-370, 1993.

[31] X. Wu and A. C. Trupp, "Spectral measurements and mixing correlation in simulated rod bundle subchannels," *International Journal of Heat and Mass Transfer,* vol. 37, no. 8, pp. 1277-1281, 1994.

[32] X. Wu, "On the transport mechanisms in simulated heterogeneous rod bundle subchannels," *Nuclear Engineering and Design,* vol. 158, no. 1, pp. 125-134, 1995.

[33] T. Krauss and L. Meyer, "Characteristics of turbulent velocity and temperature in a wall channel of a heated rod bundle," *Experimental Thermal and Fluid Science,* vol. 12, no. 1, pp. 75-86, 1996.

[34] T. Krauss and L. Meyer, "Experimental investigation of turbulent transport of momentum and energy in a heated rod bundle," *Nuclear Engineering and Design,* vol. 180, no. 3, pp. 185-206, 1998.

[35] M. S. Guellouz and S. Tavoularis, "The structure of turbulent flow in a rectangular channel containing a cylindrical rod - Part 1: Reynolds-averaged measurements," *Experimental Thermal and Fluid Science,* vol. 23, no. 1, pp. 59-73, 2000.

[36] M. S. Guellouz and S. Tavoularis, "The structure of turbulent flow in a rectangular channel containing a cylindrical rod - Part 2: phase-averaged measurements," *Experimental Thermal and Fluid Science,* vol. 23, no. 1-2, pp. 75-91, 2000.

[37] F. Baratto, S. C. C. Bailey and S. Tavoularis, "Measurements of frequencies and spatial correlations of coherent structures in rod bundle flows," *Nuclear Engineering and Design,* vol. 236, no. 17, pp. 1830-1837, 2006.

[38] N. Silin and L. Juanicó, "Experimental study on the Reynolds number

dependence of turbulent mixing in a rod bundle," *Nuclear Engineering and Design,* vol. 236, no. 18, pp. 1860-1866, 2006.

[39] E. Piot and S. Tavoularis, "Gap instability of laminar flows in eccentric annular channels," *Nuclear Engineering and Design,* vol. 241, no. 1, pp. 4615-4620, 2011.

[40] G. H. Choueiri and S. Tavoularis, "Experimental investigation of flow development and gap vortex street in an eccentric annular channel. Part 1. Overview of the flow structure," *Journal of Fluid Mechanics,* vol. 752, pp. 521-542, 2014.

[41] G. H. Choueiri and S. Tavoularis, "Experimental investigation of flow development and gap vortex street in an eccentric annular channel. Part 2. Effects of inlet conditions, diameter ratio, eccentricity and Reynolds number," *Journal of Fluid Mechanics,* vol. 768, pp. 294-315, 2015.

[42] A. Mahmood, M. Rohde, T. H. J. J. v. d. Hagen and R. F. Mudde, "Contribution of large-scale coherent structures towards the cross flow in two interconnected channels," in *13th International Topical Meeting on Nuclear Reactor Thermal Hydraulics*, 2009.

[43] Seale, " Turbulent diffusion of heat between connected flow passages Part 2," *Nuclear Engineering and Design,* vol. 54, no. 2, pp. 197-209, 1979.

[44] R. C. K. Rock and M. F. Lightstone, "A numerical investigation of turbulent interchange mixing of axial coolant flow in rod bundle geometries," *Numerical Heat Transfer, Part A: Applications,* vol. 40, no. 3, pp. 221-237, 2001.

[45] Y. K. Suh and M. F. Lightstone, "Numerical simulation of turbulent flow and mixing in a rod bundle geometry," *Nuclear Energy,* vol. 43, no. 3, pp. 153-163, 2004.

[46] X. Wu, "Numerical study on the turbulence structures in closely spaced rod bundle subchannels," *Numerical Heat Transfer, Part A: Applictions,* vol. 25,

no. 6, pp. 649-670, 1994.

[47] K. B. Lee and H. C. Jang, "A numerical prediction on the turbulent flow in closely spaced bare rod arrays by a nonlinear k−ϵ model," *Nuclear Engineering and Design*, vol. 172, no. 3, pp. 351-357, 1997.

[48] P. Carajilescov and N. E. Todreas, "Experimental and analytical study of axial turbulent flows in an interior subchannel of a bare rod bundle," *Journal of Heat Transfer,* vol. 98, no. 2, pp. 262-268, 1976.

[49] Horváth and Dressel, "Numerical simulations of square arrayed rod bundles," *Nuclear Engineering and Design,* vol. 247, pp. 168-182, 2012.

[50] E. Merzari, H. Ninokata and E. Baglietto, "Numerical simulation of flows in tight-lattice fuel bundles," *Nuclear Engineering and Design,* vol. 238, no. 7, pp. 1703-1719, 2008.

[51] D. Chang and S. Tavoularis, "Unsteady numerical simulations of turbulence and coherent structures in axial flow near a narrow gap," *Journal of Fluids Engineering,* vol. 127, no. 3, pp. 458-466, 2005.

[52] D. Chang and S. Tavoularis, "Convective heat transfer in turbulent flow near a gap," *Journal of Heat Transfer,* vol. 128, no. 7, pp. 701-708, 2006.

[53] D. Chang and S. Tavoularis, "Simulations of turbulence, heat transfer and mixing across narrow gaps between rod-bundle subchannels," *Nuclear Engineering and Design,* vol. 238, no. 1, pp. 109-123, 2008.

[54] D. Chang and S. Tavoularis, "Numerical simulations of developing flow and vortex street in a rectangular channel with a cylindrical core," *Nuclear Engineering and Design,* vol. 243, pp. 176-199, 2012.

[55] D. Chang and S. Tavoularis, "Numerical simulation of turbulent flow in a 37-rod bundle," *Nuclear Engineering and Design,* vol. 237, no. 6, pp. 575-590, 2007.

[56] A. S. Lexmond, R. F. Mudde and V. d. Haagen, "Visualization of the vortex

street and characterization of the cross flow in the gap between two subchannels," in *Proceedings of the 11th Nureth,* Avignon, France, 2005.

[57] D. Home, G. Arvanitis, M. F. Lightstone and M. S. Hamed, "Simulation of flow pulsations in a twin rectangular subchannel geometry using unsteady Reynolds Averaged Navier-Stokes modelling," *Nuclear Engineering and Design,* vol. 239, no. 12, pp. 2964-2980, 2009.

[58] D. Home and M. F. Lightstone, "Numerical investigation of quasi-periodic flow and vortex structure in a twin rectangular subchannel geometry using detached eddy," *Nuclear Engineering and Design,* vol. 270, pp. 1-20, 2014.

[59] M. Strelets, "Detached eddy simulation of massively separated flows," in *AIAA Paper*, Reno, 2011.

[60] D. Home, M. F. Lightstone and M. S. Hamed, "Validation of DES-SST Based turbulence model for a fully developed turbulent channel flow problem," *Numerical Heat Transfer, Part A: Applications,* vol. 55, no. 4, pp. 337-361, 2009.

[61] B. H. Yan, H. Y. Gu and L. Yu, "Numerical simulation of large scale vortex structure and flow pulsation in rectangular channels," *Progress in Nuclear Energy,* vol. 54, no. 1, pp. 29-35, 2012.

[62] ANSYS, Inc., "ANSYS-CFX Solver Theory Guide," November 2009. [Online]. Available: http://orange.engr.ucdavis.edu/Documentation12.1/121/CFX/xthry.pdf. [Accessed September 2015].

[63] R. Nijsing and W. Eifler, "Heat Transfer Calculations of Organic Cooled Sever-Rod Cluster Fuel Elements," *Nuclear Engineering and Design,* vol. 4, no. 3, pp. 253-275, 1966.

[64] W. Eifler and R. Nijsing, "The diminution of the local heat transfer coefficient in the contact region between two finned tubes," *unpublished work,* 1965.

[65] L. N. Bibikov, Y. D. Levchenko, V. I. Subbotin and P. A. Ushakov, "Velocity profiles of a fluid at the inlet of a close-packed bundle of rods," *Atomnaya Energiya,* vol. 35, no. 1, pp. 19-24, 1973.

[66] Ramm, Johannsen and Todreas, "Single phase transport within bare rod arrays at laminar, transition and tubulent flow conditions," *Nuclear Engineering and Design,* vol. 30, no. 2, pp. 186-204, 1974.

[67] N. Silin, L. Juanicó and D. Delmastro, "Thermal mixing between subchannels: measurement method and applications," *Nuclear Engineering and Design,* vol. 227, no. 1, pp. 51-63, 2004.

[68] C. C. Liu, Y. M. Ferng and C. K. Shih, "CFD evaluation of turbulence models for flow simulation of the fuel rod bundle with a spacer assembly," *Applied Thermal Engineering,* vol. 40, pp. 389-396, 2012.

[69] Canadian Nuclear Safety Commission, "Nuclear Power Plants," Canadian Nuclear Safety Commission, 17 11 2015. [Online]. Available: http://www.nuclearsafety.gc.ca/eng/reactors/power-plants/index.cfm. [Accessed 30 11 2015].